High-density, ultra-relativistic positron beams using the Astra-Gemini laser

Contact *g.sarri@qub.ac.uk*

G. Sarri, D. Doria, B. Dromey and M. Zepf

School of Mathematics and Physics, Queen's University Belfast, Belfast, BT7 1NN, UK

W. Schumaker, M. Vargas, A. G. R. Thomas and K. Krushelnick

Center for Ultrafast Optical Science, University of Michigan, Ann Arbor, Michigan 48109-2099, USA

K. Poder, J. Cole and Z. Najmudin

The John Adams Institute for Accelerator Science, Blackett Laboratory, Imperial College London, SW7 2AZ, UK

G. Grittani and L. Gizzi

Istituto Nazionale di Ottica, Consiglio Nazionale delle Ricerche, 56124 Pisa, Italy

Introduction

The generation of ultra-relativistic and high-quality positron beams in the laboratory is a field of research of paramount importance due to its direct relevance to a wide range of physical subjects, which include nuclear and particle physics, laboratory astrophysics, and plasma physics. Due to the obvious difficulties encountered in generating stable antimatter, and in further accelerating it to ultra-relativistic energies, this field of research has thus far been prerogative of large-scale conventional accelerators, such as the recently dismissed Large Electron-Positron Collider (LEP) [1], or the Stanford Linear Accelerator (SLAC) [2]. However, the large size (~ km) and cost of these machines is motivating the quest for alternative acceleration schemes; in this context, plasma devices are appealing candidates due to the extremely high accelerating fields that they are able to support (of the order of hundreds of GV/m, compared to the typical MV/m obtainable in conventional accelerators). Laser-plasma accelerators have already demonstrated the generation of electron beams with energy per particle reaching [3], if not exceeding [4], 1 GeV and energies per particles approaching 100 GeV are theoretically predicted [5] for the next class of high-power laser systems (such as the 10 PW Vulcan upgrade [6]).

On the other hand, laser-driven high-energy positron beams are much harder to generate. H. Chen and collaborators from the Lawrence Livermore National Laboratory (LLNL) demonstrated the possibility of generating a population of relativistic positrons by focusing a kJ-class laser ontp a mm-thick gold target [7]. Despite the intrinsic interest of these results, the positron jets obtained presented poor characteristics such as a broad divergence (cone aperture of ~ 350 mrad) and low energy per particle (E ~ 10 - 20 MeV).

We report here on recent results obtained at the Astra-Gemini laser system [8], which significantly advance the results reported by H. Chen and collaborators. Positron beams with divergence as low as a few mrad, energy as high as 600 MeV, and density as high as 10^{16} particles per centimetre cubed have in fact been experimentally obtained. These positron beams display appealing characteristics for a wide range of practical applications such as laboratory-based studies of astrophysically relevant electron-positron-ion plasma phenomena and GeV laser-driven electron-positron colliders.

The experimental setup

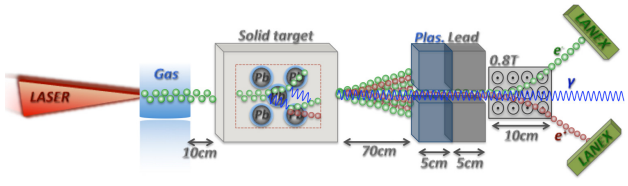

Fig.1: Sketch of the experimental setup (top-view).

The experimental setup is sketched in Fig. 1. A laser beam with a central wavelength λ_L=0.8 µm, energy on target E_L ~15 J and a duration τ_L ~ 40 fs was focused, using an f/20 off-axis parabola, (focal spot Full Width Half Maximum of 27±3 µm) onto the edge of a 20 mm wide supersonic He gasjet, doped with 3% of N_2, to a peak intensity of I_L $5x10^{19}$ Wcm^{-2}. A backing pressure of 45 bar (corresponding, once fully ionised, to an electron density of the order of 10^{19} cm^{-3}) was found to be optimum in terms of peak energy and charge of the accelerated electron beam as resulting from ionisation injection [9] in the gasjet. This interaction generated a reproducible electron beam with a broad spectrum with peak energy of the order of 600 MeV and half-angle divergence of 2 mrad. The charge carried by the electrons with an energy exceeding 160 MeV (lower limit for the spectrometer) was 0.3±0.1 nC [corresponding to $(2.0±0.6)x10^9$ electrons, see Fig. 2 for a typical series of electron spectra and for their average]. The electron beam interacted with solid targets of different composition (Pb, Ta, Mo, Sn) and thicknesses (from a few mm up to a few cm). The generated electrons and positrons were then separated and spectrally resolved by a magnetic spectrometer consisting of a 0.8T, 10 cm pair of magnets and two LANEX screens.

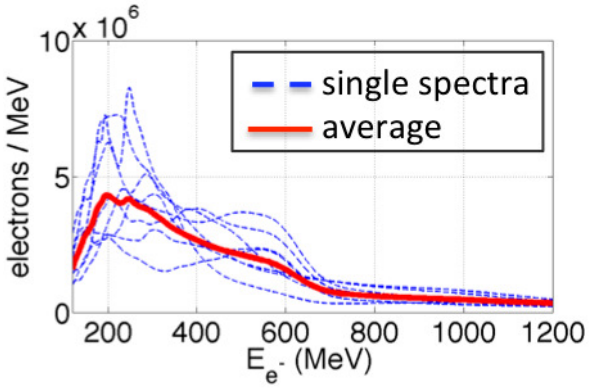

Fig.2: Series of electron spectra (dashed blue lines), as obtained during eight consecutive laser shots without the insertion of a solid target, and their average (red solid line).

Positron spectrum

Even though different materials and thicknesses were used in this experiment, we will discuss here only the results obtained from 1cm of Pb. This is in fact the solid target that produced the highest positron yield since it has the highest atomic bumber and a thickness of the order of twice the radiation length for Pb (L_{RAD} = 0.56 cm). The choice of this thickness is based on a numerical study carried out by our group, exploiting the kinetic model of electromagnetic cascade discussed in Ref. [10], which indicates that a maximum positron yield is achieved in this range of target thicknesses. Positron spectra obtained with different thicknesses (not shown) confirmed this theoretical

prediction. A typical positron spectrum obtained after the propagation of an electron beam, with a spectrum as the one depicted in Fig.2, through 1cm of Pb, is depicted in Fig. 3. As we can see, a broad spectrum, extending to approximately 600 MeV, with approximately 10^5 positrons per MeV was obtained. The measured spectrum (solid line) is in excellent agreement with the spectrum predicted by the Monte-Carlo scattering code FLUKA [11], which takes into account QED electromagnetic cascades during the propagation of an ultra-relativistic electron beam through a solid target. The number of positrons with energy exceeding 160 MeV is thus approximately $8x10^7$. Extrapolating the simulated results from FLUKA, a maximum number of relativistic positrons (E > 1 MeV) was found to be of the order of 10^9, confined in a beam with a divergence of ~ 10 mrad. It is worth noting that this yield of relativistic positrons is almost two orders of magnitude higher than what was obtained in a similar experimental campaign [12] carried out by some of the authors at the Hercules laser system hosted by the Centre for Ultrafast Optical Science at Michigan University, US [13]. By assuming that the positron beam will retain the temporal duration of the primary electron beam, which is comparable to that of the incoming laser pulse [14], and by estimating the diameter of the positron source at the rear surface of the Pb target to be, conservatively, of the order of ~ 150 μm, we obtain an overall positron density of the order of 10^{16} cm^{-3}.

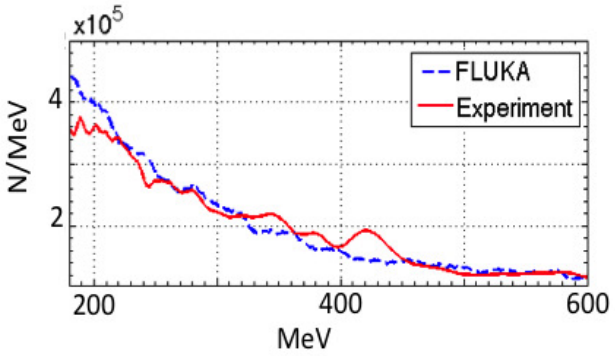

Fig.3: Typical positron spectrum, as obtained with the Gemini laser, if 1 cm of Pb were used as a solid target.

This is a striking result, since this density is only a few times lower the maximum positron density obtained at the Stanford Linear Accelerator (~$5x10^{16}$ cm^{-3}, see for instance Ref. [2]).

Conclusions

We have reported on the experimental demonstration of the feasibility of generating high-energy (E ~ 600 MeV), high-density (n ~ 10^{16} cm^{-3}), and small divergence (~ 10 mrad) positron beams from a compact all-optical setup. The positron beams obtained greatly advance previous attempts of laser-driven positron generation. The inferred density of relativsitic positrons in the beam is comparable to what achieved in large conventional accelerators such as SLAC. Moreover, the relatively low divergence of the beam suggests the possibility of implementing plasma afterburners for further acceleration of the positrons. The high density of the beam might open the pathway towards the laboratory study of electron-positron beams, in regimes of possible relevance to astrophysical electron-positron jets.

Acknowledgements

The authors are grateful for all the support received by the staff of the Central Laser Facility. The authors also acknowledge the funding schemes NSF CAREER (Grant No. 1054164) and NSF/DNDO (GrantNo. F021166). G. S. wishes to acknowledge the support from the Leverhulme Trust (Grant No. ECF-2011-383).

References

1. R. Bossart *et al.*, Report No. CERN-PS-90-56-LP (1990).
2. J. S. T. Ng *et al.*, Phys. Rev. Lett. **87**, 244801 (2001); B. E. Blue *et al.*, Phys. Rev. Lett. **90**, 214801 (2003).
3. W. P. Leemans *et al.*, Nat. Phys. **2**, 696 (2006).
4. X. Wang *et al.*, AIP Conf. Proc. **1507**, 341 (2012).
5. 100GeV W. Lu *et al.*, Phys. Rev. ST Accel. Beams **10**, 061301 (2007).
6. http://www.clf.stfc.ac.uk/New+Initiatives/The+Vulcan+10+Petawatt+Project/14684.aspx
7. H. Chen *et al.*, Phys. Rev. Lett. **102**, 105001 (2009); H. Chen *et al.*, Phys. Rev. Lett. **105**, 015003 (2010).
8. C. J. Hooker *et al.*, J. Physique IV **133**, 673 (2006).
9. C. E. Clayton *et al.*, Phys. Rev. Lett. **105**, 105003 (2010).
10. B. Rossi, *High-Energy Particles* (Prentice-Hall, New York, 1952).
11. G. Battistoni *et al.*, AIP Conf. Proceedings **896**, 31 (2007).
12. G. Sarri *et al.*, Phys. Rev. Lett. **110**, 255002 (2013).
13. V. Yanovsky *et al.*, Optics Express **16**, 2109 (2008).
14. S. P. D. Mangles *et al.*, Phys. Rev. Lett. **96**, 215001 (2006).

X-Ray measurements of the interaction of the Astra-Gemini pulse with large atomic clusters

Contact *sio05@imperial.ac.uk*

S.I. Olsson Robbie, H.F. Lowe, D. Bigourd, C. Price, S. Patankar, K. Mecseki, R.A. Smith
Blackett Laboratory, Imperial College London, London SW7 2AZ, UK

H.W. Doyle
Department of Physics, University of Oxford, Oxford, OX1 3PU, UK

S. J. Hawkes, N. Booth, D.R. Symes
Central Laser Facility, STFC Rutherford Appleton Laboratory, Chilton, Didcot, OX11 0QX, UK

J. Fyrth, E.T. Gumbrell
AWE, Aldermaston, RG7 4PR, UK

Introduction

Atomic cluster gases have been shown to be extremely efficient absorbers of high-intensity, short pulse laser energy at levels up to 90% or more compared to monoatomic gases where the coupling is typically <5% [1]. This is the result of the resonant interaction between the laser pulse and the atomic cluster and the plasmas created by this interaction are of considerable interest for applications such as scaled laboratory astrophysics experiments and laser fusion experiments.

Here we report on the first cluster interaction experiment carried out on the Gemini laser system at RALA broad range of diagnostics was fielded on this experiment to investigate not only the interaction of the laser pulse and the clusters but also the shock launched by this interaction. Here we will focus on one aspect of the diagnostic suite, the x-ray pinhole camera (XRPC) data because it captured the early time plasma created by the laser-cluster interaction, which is key to understanding the later time evolution of the system. In the past Ditmire *et al* [2] have observed similar processes but only at much lower intensities of ~10^{16} Wcm^{-2} whereas here we drive the clusters at a relativistic intensity, ~10^{19} Wcm^{-2}, and use large ~10,000 atom clusters.

Experimental Set-Up

A single beam of the Astra-Gemini laser system was focused into a volume of clusters generated by a Peter Paul valve with a large bore (1 cm diameter) nozzle. Laser energy and backing pressure scans were performed in krypton and xenon.

The x-ray pinhole camera was filtered such that it imaged the early time plasma generated by the interaction of ~10^{19} Wcm^{-3} laser pulse with large atomic clusters. An x-ray pinhole camera with a 100 µm pinhole and a magnification of x10 filtered with 25 µm Be was used so that only photons with energies above ~1 keV were detected. This reduces the time period over which the image is integrated to ~100 ps. Using this technique we were able to perform a parameter scan in energy, backing pressure and species. Narrow hot plasma filaments were observed with varying width dependent on the conditions of laser energy deposition. A clear relationship was found between the backing pressure of the gas jet (which changes both average gas density and cluster size) and the width of the observed plasma filament. This relationship was present in both krypton and xenon targets.

Early Time Plasmas

Shown in Fig. 1 is a pinhole camera image captured at full laser energy, ~13.6 J, 33 bar in krypton with an integrated lineout along the laser axis inset. The filament shown here is a smooth Gaussian with no "special" features and a width of >200 µm. This shot stands in stark contrast to the lower pressure shots in krypton where a clear dip in signal is observed along the central axis of the filament. An example of this feature is shown in Fig. 2 where the shot was taken with 13.40 J and 24.3 bar of backing pressure where the lineout of the integrated signal taken perpendicular to the propagation direction is again shown inset. In Fig. 2 the FWHM of the filament is ~300 µm and the width of the dip peak to peak is ~200 µm.

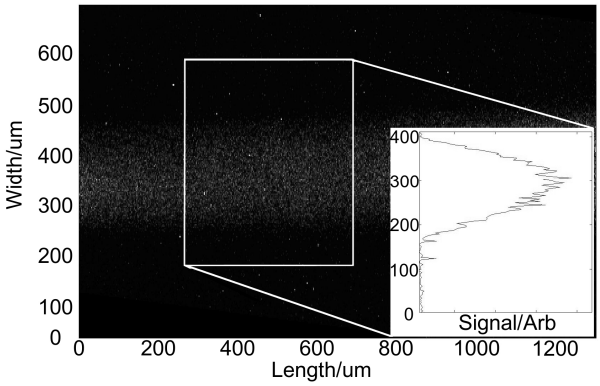

Figure 1. Plasma filament captured on the x-ray pinhole camera with ~13.6 J of energy in krypton with a backing pressure of 33 bar. The width of the filament observed here is >200 µm.

Shown in Fig. 3 are the integrated transverse lineouts for three different pressures in xenon at full energy, ~13.5 J. In this figure both the FWHM of the whole filament and the peak to peak width of the dip can clearly be seen to shrink as the backing pressure of the jet is increased, a pattern that is also repeated in krypton.

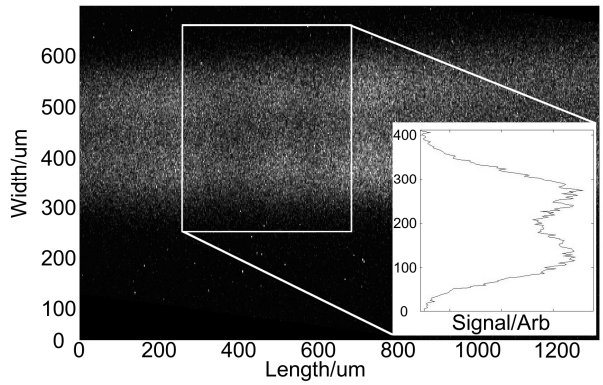

Figure 2. Plasma filament captured on the x-ray pinhole camera with ~13.6 J of energy in krypton with a backing pressure of 24.3 bar. The FWHM of the filament observed here is ~300 µm and the dip is ~200 µm.

This feature is also observed on our streaked Schlieren imaging system (used to determine blast wave radius as a function of

time [3] as shown in Fig. 3. This image was captured on a 24.3 bar shot in krypton driven with 14.13 J. The streaked Schlieren image registers a peak to peak width of 250±30 µm and the x-ray pinhole camera registers ~200 µm peak to peak for shot under the similar conditions. The slight discrepancy of the two measurements could be explained by the longer time over which the Schlieren image is integrated. resulting in the larger width as the plasma expands. Further the FWHM max is ~700 µm.

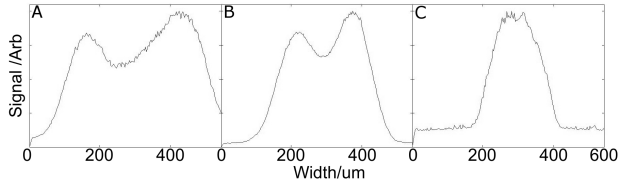

Figure 3. Integrated transverse x-ray self emission line out taken from the XRPC images over a length of 400 µm. All shots were taken in xenon at (A) 9.8 bar with 13.11 J, (B) 16.6 bar with 13.59 J and (C) 29.6 bar with 13.82 J. As is clear the filaments not only narrow with increased backing pressure but the central dip in signal is no longer present at high backing pressure.

The primary source of early time >1keV x-ray self emission in this plasma will be come from hot electrons in the medium. Therefore the images captured by the XRPC, and indeed the free electron density gradients which the streaked Schlieren captures, are linked to the local density of the electrons and their temperature. The image captured on the XRPC is of course a 2D projection of a 3D object, however the dip can be easily explained by reference to the inverse of limb darkening [4]. When looking through a chord of an emitting cylinder the edges will appear brighter because the absolute number of emitters along this path will be greater than when looking through the centre of the cylinder. This leads us to conclude that the dip feature is produced by a cylinder of hot emitting plasma with a drop in temperature or electron density at the centre. The streaked Schlieren diagnostic shows a change in density across the centre of the object indicating that there is a drop in density rather than a change in temperature.

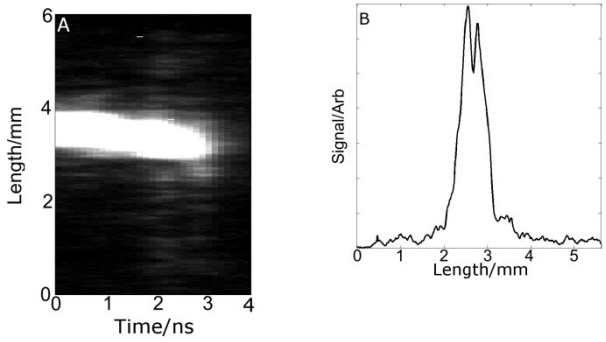

Figure 4. Shown here is the early time optical streak Schlieren image (A) captured in krypton with the gas jet backed to 24.3 bar and a drive energy of 14.13 J. B) Show the spatial signal integrated over the first 1.2 ns of the optical streak after the laser-cluster interaction.

A possible mechanism to explain this behaviour is electron blowout by the laser field itself. Here the electrons liberated by the laser pulse are pushed out of the centre of focus down the electric field gradient. This could then result in a cylindrical plasma surrounding the laser axis. However the width of this feature is linked to the density of the ambient medium. As the mass density, backing pressure, is increased the resistance to the motion of the electrons which are being pushed down the field gradient will increase. This would both narrow the overall width of the filaments and also the electron blow out from the laser axis would be impeded. This could further indicate that the shots taken at the highest mass densities begins to give an indication of the extent of the laser heated region only a matter ~100 ps after the interaction.

Conclusions

In the past, Ditmire *et al* have demonstrated using interferometry and x-ray pinhole imaging that non-local electron heat transport occurs in the first 50 ps of the laser-cluster interaction [2]. This work may provide evidence that the same behaviour was repeated with large clusters and much higher laser intensities.

In addition to this data gathered pertaining to the distribution of the early time plasma. Analysis is currently on going with the data gathered with the remaining diagnostics. This includes the measuring of the early time plasma temperature and trajectory measurements intended to investigate plasma oscillations driven by the thermal cooling instability [3], with early indications of success on both fronts. Additionally post interaction beam diagnostics have confirmed the strong absorption properties of atomic clusters under these new conditions.

Acknowledgements

We would like to gratefully acknowledge the assistance of the whole of the Astra-Gemini laser team, the Target Fabrication Team at the CLF and A.S. Moore for useful discussions.

References

1. T. Ditmire, R. A. Smith, J. W. G. Tisch, and M. H. R. Hutchinson. High intensity laser absorption by gases of atomic clusters. Physical Review Letters, 78:32121-3124, 1997.
2. T. Ditmire, E.T. Gumbrell, R.A. Smith, A. Djaoui, and M.H.R. Hutchinson. Time-Resolved study of nonlocal electron heat transport in high temperature plasmas. Physical Review Letters, 80(4):720-723, 1998.
3. A. S. Moore, E. T. Gumbrell, J. Lazarus, M. Hohenberger, J. S. Robinson, R. A. Smith, T. J. A. Plant, D. R. Symes, and M. Dunne, Full-Trajectory Diagnosis of Laser-Driven Radiative Blast Waves in Search of Thermal Plasma Instabilities. Physical Review Letters, 2008, 100, 055001.
4. H. Neckel and D. Labs. Solar limb darkening 19861990. Solar Physics, 153:91-114, 1994.

Relativistic electron beams with low energy spread by ionisation injection in a structured gas cell

Contact *n.carreira-lopes@imperial.ac.uk*

N. C. Lopes

GoLP/Centro de Fisica dos Plasmas, Instituto Superior Tecnico, Lisboa, Portugal and

The John Adams Institute for Accelerator Science, Blackett Laboratory, Imperial College London, SW7 2AZ, UK

J. M. Cole, A. E. Dangor, N. P. Dover, S. Kneip, S. P. D. Mangles, H. Nakamura, K. Poder, M. J. V. Streeter, J. C. Wood, Z. Najmudin

The John Adams Institute for Accelerator Science, Blackett Laboratory, Imperial College London, SW7 2AZ, UK

N. Booth, D. R. Symes

Central Laser Facility, STFC Rutherford Appleton Laboratory, Chilton, Didcot, OX11 0QX, UK

S. Hillenbrand

CERN, Geneva, Switzerland and KIT, Karlsruhe, Germany

J. Osterhoff, C. A. J. Palmer, L. Schaper

DESY, Hamburg, Germany and Plasma Accelerator Group, University of Hamburg, 20148 Hamburg, Germany

Introduction

The parameters of electron bunches produced by Laser driven Wakefield Plasma Accelerators (LWFA) [1] are improving with the progress of short pulse laser technology and techniques to inject those electron bunches into the accelerating plasma structure. Since the first demonstration of the capability of LWFA to produce mono-energetic electron bunches [2-4], several new injection techniques have been proposed and tested aiming to improve the beam quality, reproducibility, and bunch charge: colliding pulses [5], density variations [6] and ionisation injection [7,8]. Ionisation injection can be used to significantly decrease the laser intensity threshold for electron injection. In a single pulse configuration, the same laser pulse that is used to drive the wakefield is also used to ionise some of the electrons of a gas with an atomic number higher than the background gas (hydrogen or helium). When the laser pulse length is a significant fraction of the "plasma bubble" length, the ionisation of these electrons may happen inside that "plasma bubble", in a region of the wakefield potential where trapping by the relativistic structure is possible. For the Astra-Gemini laser pulse parameters, a background density close to 1×10^{18} cm^{-3} of hydrogen or helium provides the adequate relation between the pulse length and the "plasma bubble size" so that ionisation injection can occur for "impurity" atoms with appropriate ionisation levels. Ideally, the impurity gas will have the outer electrons ionised (field ionisation) well before the plasma bubble and some of the inner electrons ionised near the maximum intensity of the laser pulse near the centre of the "plasma bubble" so they can be trapped. Therefore, a gas with low atomic number (but higher than the background gas) with a significant ionisation potential step after the first few ionisation levels will be adequate. In this experiment we used a mix of helium and nitrogen. The spatial limitation of the "impurity" gases [9] was also used to reduce the energy spread of the resulting electron beams to below 2%.

In this report we describe the generation of low energy spread electron bunches by ionisation injection in a structured gas cell. The main feature of this cell is the existence of a small compartment where the mixed gas can be locally injected into the wakefield. This feature greatly diminishes the diffusion of the 'impurity' gas throughout the rest of the cell length, leading to the reduction of the final energy spread of the electron beams. The spatial limitation of the injection region may also enhance the final energy of the accelerator by reducing the erosion of the laser pulse due to extended lengths of impurity gas ionisation.

Experimental setup for ionisation injection

The experimental results were obtained in the Astra-Gemini target area. A schematic of the experimental setup is presented in figure 1. One of the Astra-Gemini laser beams was *f*/20 focused into the gas cell. The gas cell consisted of a sequence of three compartments separated by thin plates with 300 micron apertures coincident with the laser axis. The ends of the gas cell consisted of metallic cones with apexes and apertures also coincident with the laser axis. A continuous flow of gas was injected in each compartment starting 500 ms before each laser shot by opening a solenoid valve. The gas density during the laser shots could be controlled through the pressure of the gas before the gas valve.

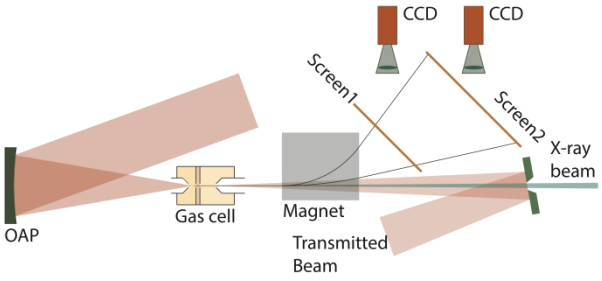

Figure 1: Experimental Setup schematic.

The plasma density in the gas cell was measured by interferometry using a fraction of the second Astra-Gemini laser beam. This probe beam was propagated transversely to the main optical axis using two optical windows in the sides of the gas cell (not shown in schematic).

The energy of the accelerated electrons was measured by analysing the deflection of the beam by a static magnetic field in the gap in a magnetic circuit created using permanent magnets. The deflection, proportional to the inverse of electron momenta, was measured by imaging two scintillating screens (Lanex). For a detailed description of this spectrometer see reference [10].

The exit mode of the gas cell was imaged into a CCD camera and a spectrometer (not shown in schematic). The first mirror following the interaction contained a 1 cm aperture (*f*/150) from where it was possible to extract the x-ray beam produced by the betatron motion of the electron beam in the plasma.

The laser beam

One of the Astra-Gemini laser beams was used to drive the LWFA. The pulse duration was measured between 42 and 45 fs FWHM using a SPIDER diagnostic. The wavefront was corrected by a deformable mirror to improve the beam profile at focus. A typical focal spot of the partially-amplified laser beam is presented in figure 2. The spot size was w_0 ($1/e^2$) = 16.7 μm and the energy contained under the correspondent gaussian fit was 56.9 %. Therefore, assuming the same temporal and spatial shape for the amplified pulse, the peak intensity corresponds to a normalised vector potential a_0 between 3.9 and 4.8 for laser pulse energies between 12 and 16 J.

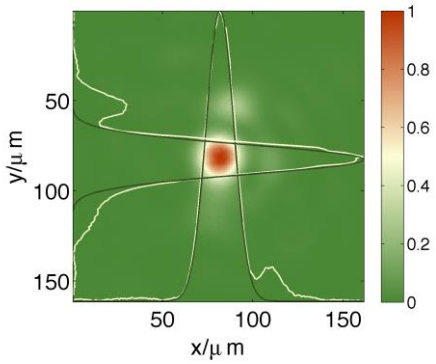

Figure 2: Focal spot of the partially amplified beam.

The plasma target

The first and last compartment of the cell (yellow in figure 1) was injected with pure helium. The middle compartment (red in figure 1) was injected with a mix of helium (99%) and nitrogen (1%). Each gas was injected into the cells continuously by opening a solenoid valve from 500 ms before the laser shots. The plasma density was controlled by changing the pressure in the tubes before the valves for each gas.

A transverse interferometry picture of the plasma target is presented in figure 3. The analysis of the interferogram by applying an Abel transformation method to the retrieved phase indicates a plasma density of 1.8×10^{18} cm^{-3} in the third compartment.

For this shot the pressures (before the solenoid valve) were 400 mbar for pure helium and 50 mbar for the mix. This set of two pressures minimise the energy spread of the resulting electron beam.

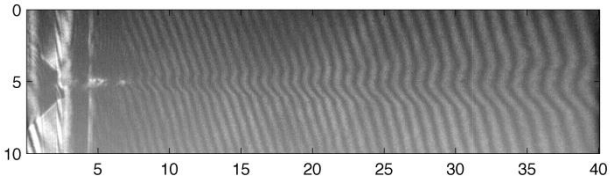

Figure 3: Typical transverse interferometry picture of the plasma. The units are mm.

The resulting electron beams

The interaction of the laser beam with the gas target resulted in the production of a low divergence mono-energetic electron beam. The energy spectra of these beams can be measured using the scintillating screens. In figure 4 we present an image obtained in the second screen of one of the best quality electron beams obtained in this experiment (the interferogram of figure 3 and the electron spectra of figure 4 correspond to the same shot). Preliminary analysis of the spectrum presented in figure 4 result in a central energy of 800.5 MeV with an energy spread (FWHM) of 13.0 MeV (after subtraction of the beam diameter) resulting in an energy spread ($\Delta E/E$) of 1.6 %. The charge contained in the spot is ≈ 30 pC. We note that at these low densities, an electron beam was not usually produced if there was no impurity region.

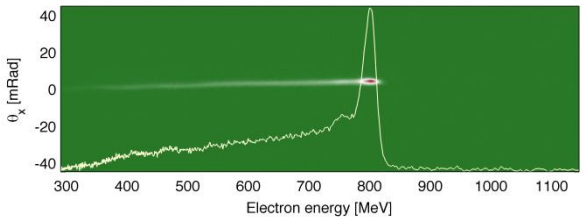

Figure 4: Energy spectrum of a mono-energetic electron beam obtained in the second screen. The added line corresponds to a vertical integration (along constant energy) of the scintillation signal. The intensity is in arbitrary units.

Spectra with energy spread similar to the one in figure 4 were produced with central energies between 650 MeV and 860 MeV, approximately 28% variation. This variation is likely to be due to a number of parameters such as change in focal spot distribution and laser energy, which arise because at these high laser intensities, non-linear evolution of the pulse is still significant. The maximum amount of injected charge was obtained for a precise value of laser pulse energy (12.6 ± 0.2 J for three shots).

Discussion

The introduction of the gas mix containing 1% of nitrogen resulted in good quality electron beams (lower energy spread and beam divergence) with tens of pC. These electron beams (with similar signatures to the one presented in figure 4) were obtained for a specific plasma density and the maximum bunch charge was produced for a specific laser pulse energy. The fact that no such beams were typically observed by self-injection at comparable densities, suggests the trapping of charge by ionisation injection. If we assume that the impurity corresponds to 1% of the density measured in the third cell compartment and that it exists only in the 650 micron corresponding to the middle compartment added by half of the separation plates, this would correspond to total amount of nitrogen of 1.2×10^{14} atoms/cm^2. The laser pulse used in the experiments, before depletion, is able to ionise the last two nitrogen electrons (6^{th} and 7^{th}) for a diameter of at least 20 micron while the remaining five electrons are easily ionised outside the "plasma bubble". The 30 pC maximum charge obtained on the best shots would require an injection diameter of approximately 10 μm, assuming injection of both the 6th and 7th nitrogen electrons. This corresponds to about half of the laser spot size and the expected diameter of the "plasma bubble" in the region of the middle cell. Therefore a possible scenario for the production of the charge detected in the scintillation screen presented in figure 4 (and other similar shots) is the injection of the totality of the nitrogen electrons resulting from the 6^{th} and 7^{th} nitrogen ionisation on a cylinder with half of the "plasma bubble diameter" and the length of the middle compartment.

Conclusion

In this work we have demonstrated he capability of LWFA with ionisation injection in a structured gas cell to produce electron bunches with energy spreads below 2% with charges up to 30 pC with energies close to 1 GeV.

Acknowledgements

This work was funded by The John Adams Institute, EPSRC grant number EP/H00601X/1, Fundação para a Ciência e Tecnologia – Portugal, European Commission, FP7 contract number 283745 (CRISP) and the German BmBF via a Wolfgang Gentner grant. We thank the engineering staff at the CLF for their invaluable assistance.

References

1. T. Tajima and J. M. Dawson, Phys. Rev. Lett. 43, 267 (1979)
2. S.P.D. Mangles et al., Nature 431, 535 (2004)
3. C.G.R. Geddes et al., Nature 431, 538 (2004)
4. J. Faure et al., Nature 431, 541 (2004)
5. J. Faure, et al., Nature 444, 737 (2006)
6. A. Buck et al., Phys. Rev. Lett. 110, 185006 (2013)
7. A. Pack et al., Phys. Rev. Lett. 104, 025003 (2010)
8. C. McGuffey et al., Phys. Rev. Lett. 104, 025004 (2010)
9. B. B. Pollock et al., Phys. Rev. Lett. 107, 045001 (2011)
10. M. S. Bloom et al., CLF annual report (2012)

Extended guiding of ultra-intense laser pulses up to 4 cm in a gas cell

Contact *k.poder12@imperial.ac.uk*

K. Poder, J. M. Cole, A. E. Dangor, N. P. Dover, S. Kneip, S. P. D. Mangles, H. Nakamura, M.J.V. Streeter, J. C. Wood, Z. Najmudin

The John Adams Institute for Accelerator Science, Blackett Laboratory, Imperial College London, SW7 2AZ, UK

C.A.J. Palmer, L. Shaper, J. Osterhoff

DESY, Hamburg, Germany and Plasma Accelerator Group, University of Hamburg, 20148 Hamburg, Germany

N. C. Lopes

GoLP/Centro de Fisica dos Plasmas, Instituto Superior Tecnico, Lisboa, Portugal and The John Adams Institute for Accelerator Science, Blackett Laboratory, Imperial College London, SW7 2AZ, UK

D. R. Symes, P. S. Foster, S. J. Hawkes, C. J. Hooker, B. Parry, O. Chekhlov, Y. Tang, P. P. Rajeev

Central Laser Facility, STFC Rutherford Appleton Laboratory, Chilton, Didcot, OX11 0QX, UK

Introduction

Laser plasma electron accelerators have undergone huge developments since being conceived in late 1970s [1]. The production of multi-GeV beams in cm scale accelerators has been reported recently [2]. These energies are achieved by maintaining an accelerating gradient of the order of 100 GVm^{-1} for most of the length of the accelerator. However, as natural diffraction happens on length scales of ~1 mm, some form of guiding is needed to obtain a sufficiently long interaction length. This can be done by either employing a guiding structure [3] or using the nonlinear focusing response of the plasma itself to guide the pulse [4]. The latter scheme is of interest due the simplicity of the setup, and has been investigated in detail before in gas jet targets [5]. Recently, there has been great interest in using gas cell targets, due to their potential for greater uniformity and possibly creating longer interaction lengths [6]. Indeed electron acceleration with such targets has already shown greater reproducibility. Here, we report self-guiding in a new gas cell designed for Astra Gemini experiments with lengths up to 39 mm.

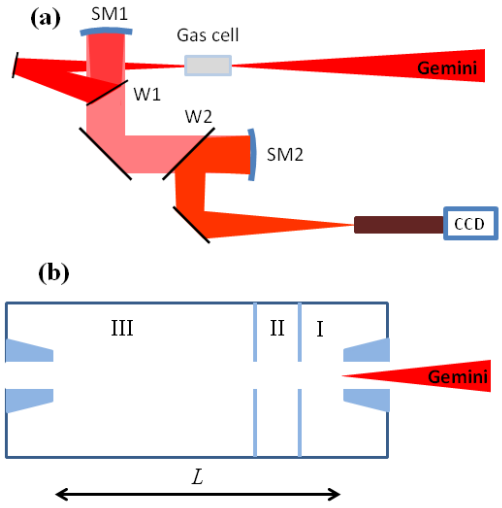

Figure 1: (a) The schematic setup of the experiment. The laser is focused onto the entrance of a gas cell. The pulse is reflected onto a spherical mirror SM1, which recollimates the beam. It is then transported out of vacuum and refocused onto the exit mode diagnostic with SM2. (b) Schematic of the gas cell used in the experiment, showing the three compartments and defining the total plasma length L.

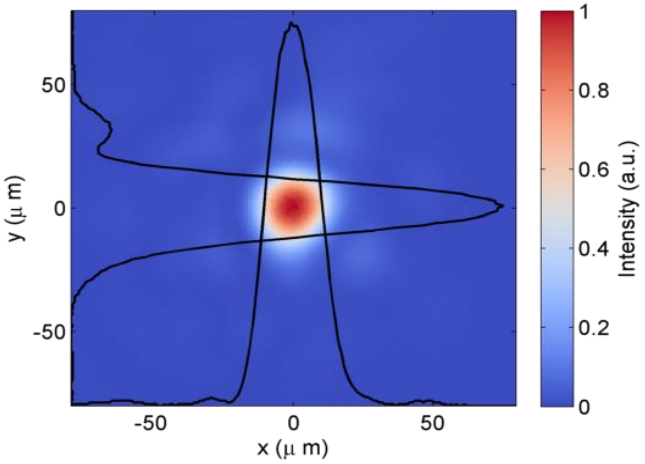

Figure 2: A typical focal spot of the f/20 optic.

Experimental setup

The experiment was performed on the Astra-Gemini laser, delivering pulses of energy ~14 J and temporal duration of ~45 fs full-width-half-maximum (FWHM), yielding a power of ~350 TW, which gives a minimum plasma density for self-guiding of 9×10^{16} cm^{-3}. The pulses were focused onto the entrance of a variable length gas cell using an *f*/20 off-axis parabola. The pulse exiting the plasma was collected with an *f*/10 spherical mirror and refocused onto a 10× apochromatic microscope objective, as schematically depicted in Figure 1a. The resolution limit of the exit mode diagnostic was 10 μm and the field of view of the 16-bit CCD detector was 1.2×1.2 mm.

The gas cell comprised of three compartments, with 500 micron holes separating the three compartments and interfacing the gas cell with vacuum, as schematically shown in Figure 1b. The neutral helium gas backing pressures in each compartment was independently variable. The total length of the cell was varied by changing the length of the third compartment, resulting in total plasma lengths in the range of 5-39 mm.

A typical focal spot is depicted in Figure 2. The 1/e^2 semi-axes of intensity are 20.0 and 16.7 microns, yielding an average radius $r=\sqrt{a\times b}$ of 18.2 μm. This corresponds to peak intensity of $2.8\cdot10^{19}$ Wcm^{-2} and normalised vector potential $a_0=3.6$. The Rayleigh range, the length over which the beam diffracts to increase its radius $\sqrt{2}$ times, is given by $z_R=M^2\pi w_0^{\,2}/\lambda$. For the spot depicted in Figure 2, the Rayleigh range is 1.3 mm, as calculated from the average radius.

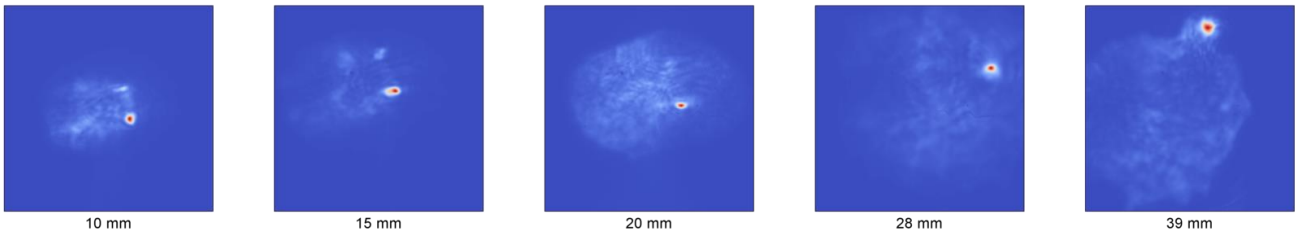

Figure 3: Exit modes recorded for different lengths of the plasma cell. All images have same spatial scale of 1.2×1.2 mm.

Results

Images of the exit mode imaging the laser beam spatial profile as it exits the plasma are shown in Figure 3. The profiles shown are for gas cell lengths of L = 10, 15, 20, 28 and 39 mm, corresponding to 7.7, 12, 15, 22 and 30 Rayleigh ranges, respectively. Plasma density in the presented shots ranged from $3{\cdot}10^{18}$ cm^{-3} for the shortest cell length to ~ $1.5{\cdot}10^{18}$ cm^{-3} in the longest cell, which is much higher than the threshold for self-guiding calculated earlier. All images depict the entire field of view of 1.2×1.2 mm and have been normalised to their individual intensity peaks. The halo around the filament represents the size the unguided beam, diffracting at the cone angle of the original *f*/20, except in the cases of the two longest cell lengths, where the exit aperture of the gas cell clips the beam. However, given the propagation length of 30 Rayleigh ranges and the initial spot size, the beam would be of diameter ~1.1 mm, making the imposed clip very small.

Cell length (mm)	w_{0x} *(μm)*	w_{0y} *(μm)*	*r (μm)*	λ_p
10 mm	34.8	39.1	36.9	39.7
15 mm	61.3	30.0	42.9	43.4
20 mm	41.7	24.7	32.1	43.4
28 mm	42.8	33.3	37.8	48.6
39 mm	57.1	56.8	56.9	56.1

Table 1: The guided filament semi-axes at the exit plane with the average radius for different gas cell lengths along with the relativistic plasma wavelength for the densities used for each cell length.

Dimensions of the filaments exiting the different length gas cells are gathered into Table 1. As can be seen, all the filaments are of the size of the relativistic plasma wave wavelength λ_p, suggesting that they are generated by relativistic self-focusing. To further quantify this, we can, using the pulse front erosion model put forward in Ref [7], estimate the exiting guided energy by assuming a constant etching rate of

$$\upsilon = \left(\frac{\omega_0}{\omega_p} \right)^2 c$$

This leads to exiting energy fractions of 0.46, 0.25, 0.06, 0.02 and 0.02 for each of the cell lengths. Even with the assumption that there is no pulse compression in the plasma, this would mean the laser is still above P_c = 17.4 (n_c/n_e) for the three shorter cell lengths. For the two longer cells, the laser would need to be compressed by 1.8 and 3.7 times, which is reasonable in light of previous studies [8].

The emergence of the guided beamlets at non-central positions can be linked to asymmetry of the initial spot. In particular, for a near top hat near-beam profile, there is generally an enhancement of intensity near the edges of the beam after the optimum focus positions. Initial unguided light would form filaments travelling near the edges of the beam which may then attract any following high intensity filaments, as appears to be the case here.

Conclusions

Self-guiding of an ultra-intense laser spot to lengths greatly exceeding the natural beam diffraction length has been demonstrated. The ~350 TW laser was successfully guided up to 39 mm. Although for n_e ~ $1.5{\cdot}10^{18}$ cm^{-3}, the dephasing length is 1.3 cm, using slightly lower plasma densities may offer similar guiding performance with a longer dephasing length, thus opening the prospect of multi-GeV electron gains with sub-petawatt lasers.

Acknowledgements

This work was funded by The John Adams Institute, EPSRC and grant number EP/H00601X/1. We would like to thank the engineering team on Astra-Gemini for their assistance.

References

1. T. Tajima, J. Dawson, Phys. Rev. Lett. **43**, 267 (1979)
2. X. Wang *et al.*, Nat. Comm. **4**, 1988 (2013)
3. W. Leemans *et al.*, Nat. Phys. **2**, 696 (2006)
4. S. Kneip *et al.*, Phys. Rev. Lett. **103**, 035002 (2009)
5. A.G.R. Thomas *et al.*, Phys. Rev. Lett. **98**, 095004 (2007), J. Ralph *et al.*, Phys. Rev. Lett. **102**, 175003 (2009)
6. J. Osterhoff *et al.*, Phys. Rev. Lett. **101**, 085002 (2008)
7. C. Decker *et al.*, Phys. Plas. **5**, 2047 (1996)
8. J. Schreiber *et al.*, Phys. Rev. Lett. **105**, 235003 (2010)

Optically-Stimulated Raman Side Scatter in a Laser Wakefield Accelerator

Contact *j.cole11@imperial.ac.uk*

J. M. Cole, M. J. V. Streeter, N. Dover, H. Nakamura, K. Poder, J. Wood, S. P. D. Mangles, Z. Najmudin

The John Adams Institute for Accelerator Science, Blackett Laboratory, Imperial College London, SW7 2AZ, UK

N. C. Lopes

GoLP/Centro de Fisica dos Plasmas, Instituto Superior Tecnico, Lisboa, Portugal and

The John Adams Institute, Blackett Laboratory, Imperial College London, London SW7 2BZ, United Kingdom

C. A. J. Palmer, L. Schaper, J. Osterhoff

Plasma Accelerator Group, University of Hamburg, 20148 Hamburg, Germany

S. Hillenbrand, A. S. Müller

KIT, Karlsruhe, Germany

R. Assmann, R. Jones

CERN, Geneva, Switzerland

G. Sarri, D. Doria, M. Zepf

School of Mathematics and Physics, Queen's University Belfast, Belfast, BT7 1NN, UK

W. Schumaker, M. Vargas, A. G. R. Thomas, K. Krushelnick

Center for Ultrafast Optical Science, University of Michigan, Ann Arbor, Michigan 48109-2099, USA

N. Booth, P. S. Foster, D. R. Symes, O. Chekhlov, S. J. Hawkes, C. J. Hooker

Central Laser Facility, STFC Rutherford Appleton Laboratory, Chilton, Didcot, OX11 0QX, UK

Introduction

Energetic charged particle beams enjoy many applications, from fundamental particle physics to medical imaging and therapy. Acceleration of electrons using conventional RF-based techniques requires long accelerator lengths however, especially when the required energies reach the GeV level. Laser-driven plasma-based accelerators[1] offer an attractive alternative due to their much shorter associated acceleration lengths, and the technique of Laser Wakefield Acceleration (LWFA) has achieved electron beam energies of GeV levels[2].

In a LWFA an intense laser pulse ($I > 10^{18}$ Wcm^{-2}) is focused into a neutral medium – often a supersonic gas jet – which is ionised into a plasma by the leading edge of the pulse. As the main body of the pulse enters the plasma it drives a relativistic plasma electron wave through the action of the ponderomotive force, which travels along with the laser at the electromagnetic group velocity. The pulse is in turn shaped by the plasma – relativistic self-focusing[3] causes the pulse to contract until it matches the plasma wavelength, and the electron-depleted cavity behind the pulse stimulates temporal pulse compression[4].

This period of pulse modification occurs soon after the laser enters the plasma, and can be accompanied by the onset of various electron parametric instabilities. Raman scattering in particular, where a laser photon decays into a plasmon and a scattered photon[5], is often observed early in the laser-plasma interaction – the self-emission region. We report here on a set of experiments where Raman scattering was observed at an angle close to perpendicular to the drive beam (Raman Side Scattering – RSS). The RSS signal was dramatically enhanced by the introduction of a much weaker transverse probe beam, and we attempt to understand this process with a theoretical model.

Experimental Setup

The two experiments reported on here were based around electron acceleration through LWFA, and took place on the Astra-Gemini laser. Figure 1 shows a simplified schematic of the experimental setup, omitting those diagnostics not relevant to discussion. The 150 mm-diameter 800 nm-wavelength full-power South beam was focused to a near-diffraction-limited focal spot of 20 μm FWHM using a 3 m focal length parabolic mirror. A deformable mirror was inserted in the South beamline, and a daily calibration took place to keep the RMS wavefront error < λ/20. The South beam was then focused into a supersonic helium gas jet of 15 mm inner diameter with vertical polarisation. The neutral gas density profile of the jet was found interferometrically to consist of linear 1.5 mm ramps at the edges with an approximately constant-density plateau across the centre of the jet. The on-target energy reached 15 J, which together with a temporal FWHM of 37-45 fs generated a peak a_0 = 4-5.

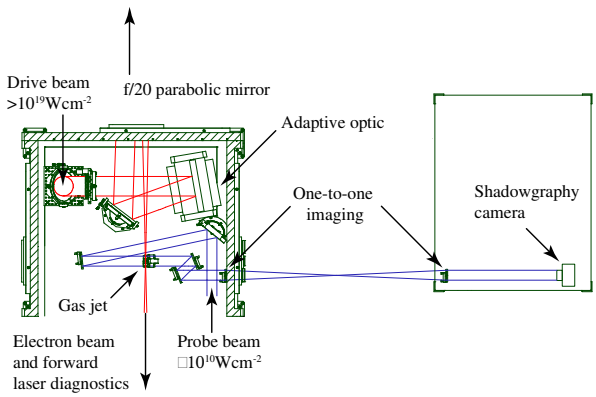

Figure 1: Layout of South end of Gemini target area

The North beam was used as a low-intensity probe in both experiments, passing perpendicularly through the gas jet and out of the interaction chamber. Two f / 11 achromatic lenses were used to perform one-to-one imaging of the interaction onto a set of probe diagnostics. Shadowgraphy and Mach-Zehnder interferometry were performed with a pair of cooled 16-bit cameras. The large CCDs allowed imaging of the full extent of the gas jet. The North beam geometry was slightly different between experiments causing the polarisation at the target to be vertical in one, and horizontal in the other.

The forward diagnostics differed between experiments, but both confirmed the production of low-divergence electron beams at GeV energies, indicating the LWFA was operating near peak performance.

Scattered Filaments

When optimising the LWFA it is common to adjust the position of the laser focus (z-position) relative to the front of the gas jet. When the z-position was unoptimised and the electron beam was poor, filaments were observed emerging from the region of self-emission – a particularly striking example is displayed in Fig. 2. Relativistic self-focusing is associated with the RSS instability[6], in particular when the focal spot entering the plasma is far from the matched spot size the period of self-focusing is more prolonged, stimulating the associated RSS process. To determine whether the filaments are indeed related to Raman scatter it is possible to find an angle of peak growth rate for 3-wave Raman Forward Scatter (RFS) – this is scatter where the electromagnetic wave is scattered predominantly in the forward direction. Assuming conservation of momentum $\mathbf{k}_0 = \mathbf{k}_s + \mathbf{k}$, where the laser photon $\mathbf{k}_0$ can be thought to decay into a scattered photon $\mathbf{k}_s$ and a plasma wave $\mathbf{k}$.

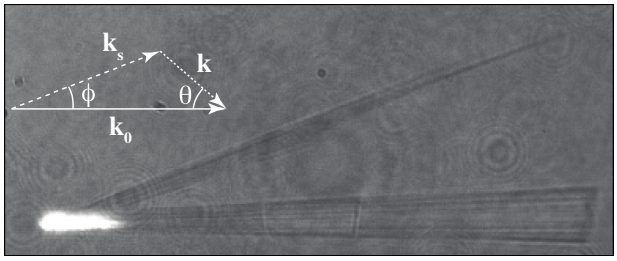

Figure 2: Shadowgram featuring very strong scattering

The angle ϕ between the pump and the scatter is then given by[7,8]

$$\sin\phi = \sqrt{\frac{2\omega_p}{\omega_0\sqrt{\gamma}}}, \quad \gamma = 1 + \frac{a_0^2}{2}$$

where ω_p is the plasma frequency, ω_0 is the laser frequency and γ is the relativistic factor associated with the pump beam.
Fig. 3 plots the measured angle against this relation for different assumed values of a_0. The scatter angle does increase with density which indicates that RFS is the likely cause for the observed filaments. However the value of a_0 which best matches the observed angles is significantly lower than the measured vacuum a_0, and the higher self-focused plasma a_0. Features resembling Raman-scattered plasma waves are often observed in simulations emanating from regions outside of the main body of the drive pulse, so it is possible that the effective relativistic factor felt by the scattering electrons is significantly lower than the peak value.

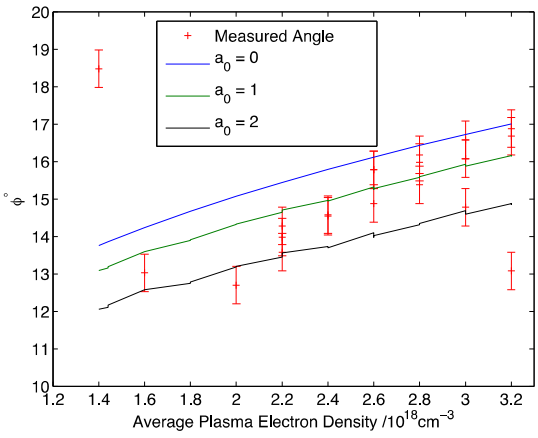

Figure 3: RSS filament angles as a function of plasma electron density

Enhanced Scatter With Timed Probe

When commissioning the transverse diagnostics in the early stages of the experiment the relative timing between the North and South beams was gradually adjusted. As the North (probe) beam was delayed, it crossed the plasma later in the interaction and the plasma channel was observed at different stages of evolution. The two laser pulses, drive and probe, were in general made to cross after the end of the gas jet to ensure the probe was late enough to see the entire plasma channel. The observed self-emission however would be expected to be independent of the probe timing and the transverse diagnostics should see the time-integrated emission over the entire lifetime of the plasma (providing the exposure time is significantly longer than the lifetime).

In this experiment though, the beam timing process caused the two pulses to overlap within the self-emission region of the plasma. This caused a striking enhancement in the amount of light seen to be produced from this region, as is shown in Fig. 4. In this series of shots the plasma electron density was 3.4×10^{18} cm^{-3} and the laser was focused 2 mm into the gas jet. All parameters were kept fixed except for the relative delay between the two beams.

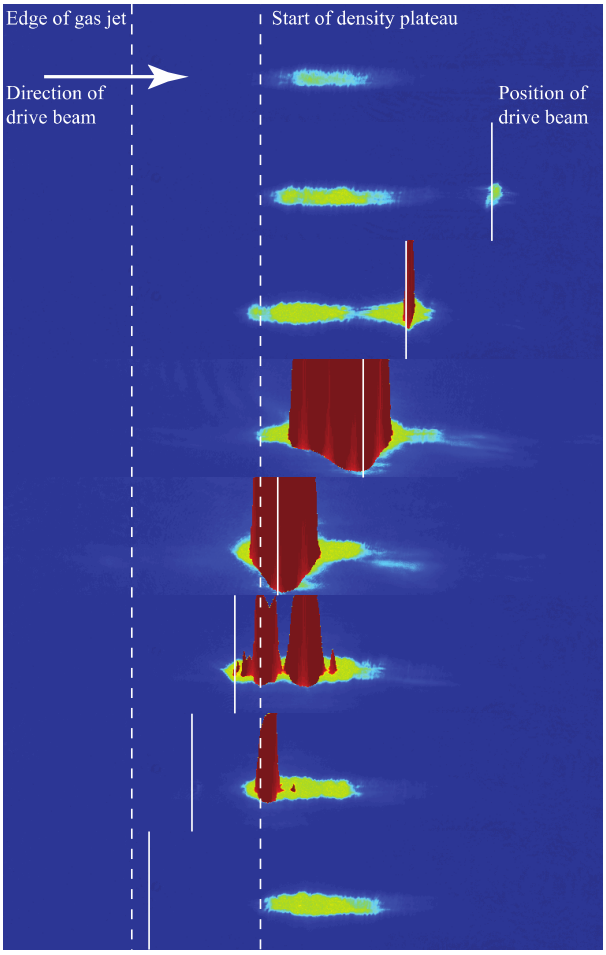

Figure 4: Shadowgram probe-delay series

What is plotted is a series of 'shadowgrams', though the dominant feature is the self-emission. Overlaid white bars denote the position of the drive beam in each image, and the dotted lines show the extent of the plasma. The colour scale abruptly changes to red at the readout limit of the CCD to show where the camera begins to saturate. It is seen that as the probe is timed gradually earlier there is much more light produced from the self-emission region. When the probe is timed to be completely inside this region the CCD is hugely saturated. Fortunately secondary reflections appear elsewhere on the large CCD which do not saturate, and therefore permit quantitative analysis.

The intriguing nature of this phenomenon was further investigated in a second run with the drive and probe beams

polarised in opposite directions – the drive vertical as before but the probe horizontal. In this case the enhancement in scatter was significantly less prominent, though still measureable. Immediately preceding the timing measurements a set of shots were taken to assess the location of the scattered RFS filaments. By tracking the filaments back to the drive beam axis it is possible to build up a distribution of the filament sources. These results are plotted in Fig. 5 where the large disparity between the two polarisation cases is immediately apparent.

Enhancement is seen in an approximately 3mm-long window inside the self-emission region, correlating with the RFS filament sources. From spectroscopic measurements performed on the two experiments the enhanced emission is seen to be centred away from 800 nm, though the spectral resolution wasn't sufficient to determine the scaling with plasma density.

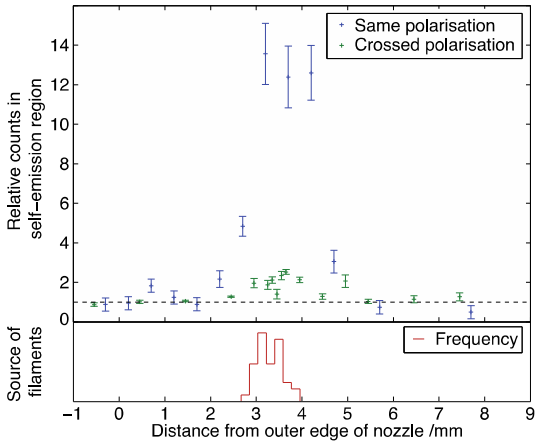

Figure 5: Relative enhancement of counts in self-emission region as a function of polarisation

These two facts together suggest that this scattered light is Raman scatter in the perpendicular direction, and is strongly stimulated by the presence of a relatively weak probe beam.
To investigate this theory a parametric instability analysis was developed which generalises that presented in Drake[5] and Sakharov[9]. The process was to assume the existence of a drive and probe beam ($\mathbf{k}_0$ and $\mathbf{k}_t$ respectively) crossing in a plasma, driving an electron wave $\mathbf{k}$. Radiation may be scattered from both the drive and probe beam, with both types of scatter able to become resonant and drive an exponentially-growing plasma wave. The plasma wave is defined by its wavevector $\mathbf{k}$, parameterised by a magnitude $k = |\mathbf{k}|$ and a direction relative to the drive beam θ – Fig. 2 shows the scattering geometry. With the plasma wave wavevector defined, the angle the scattered light makes with the drive beam ϕ can be calculated from $\mathbf{k}_s = \mathbf{k}_0 - \mathbf{k}$. Fig. 6 shows in the (k, θ) plane the change in the growth rate of plasma waves given the presence of an additional probe beam at 90° to the pump. Different plasma waves will scatter light at different angles ϕ, and the range of ϕ that were collected in our experiments are superimposed as curved black contours.

It is seen that plasma waves near 50° to the pump experience a change in growth rate $\approx 0.3\omega_p$, and are of the right wavelength to scatter pump light into the collection angle of our lens. At the plasma densities investigated in our experiment, exponentiating at this rate over 15μm would cause an order of magnitude increase of the plasma wave and scattered light amplitudes, similar to what we see in experiment.

Conclusions

Raman-scattered light and its effects on the plasma channel were found to be a useful indicator of laser focusing position. The angle of scattered filaments changed with plasma density in a way that suggested they were a result of RFS, but the required electron relativistic factor suggests the scattering occurs away from the centre of the drive pulse.

When spatiotemporally overlapping the probe and pump beams the plasma self-emission increased dramatically, and in a way which was consistent with the probe beam stimulating the Raman scattering process. Linear instability analysis suggests the presence of a transverse probe stimulates the growth of plasma waves of the right parameters to scatter extra pump light into the probe direction.

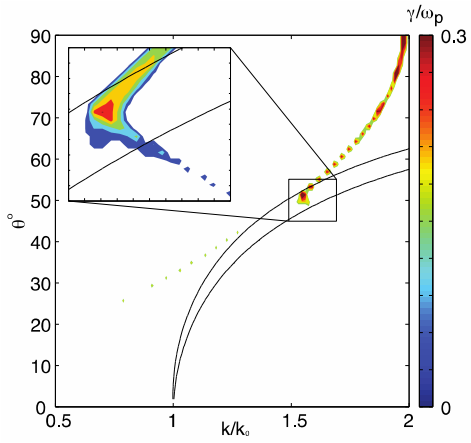

Figure 6: Change in growth rate with presence of probe. Black contours denote lens collection angle

Acknowledgements

The authors would like to thank the CLF staff running the laser and assisting in the target area, and those proving technical support throughout the experiment.

References

1. Tajima, T. & Dawson, J. M. Laser electron accelerator. *Physical Review Letters* **43**, 267–270 (1979).

2. Kneip, S. *et al.* Near-GeV Acceleration of Electrons by a Nonlinear Plasma Wave Driven by a Self-Guided Laser Pulse. *Physical Review Letters* **103**, 035002 (2009).

3. Max, C., Arons, J. & Langdon, A. Self-Modulation and Self-Focusing of Electromagnetic Waves in Plasmas. *Physical Review Letters* 209–212 (1974).

4. Faure, J. *et al.* Observation of Laser-Pulse Shortening in Nonlinear Plasma Waves. *Physical Review Letters* **95**, 205003 (2005).

5. Drake, J. F. Parametric instabilities of electromagnetic waves in plasmas. *Physics of Fluids* **17**, 778 (1974).

6. Antonsen, T. M. & Mora, P. Self-focusing and Raman scattering of laser pulses in tenuous plasmas. *Physics of Fluids B: Plasma Physics* **5**, 1440 (1993).

7. Matsuoka, T. *et al.* Stimulated Raman Side Scattering in Laser Wakefield Acceleration. *Physical Review Letters* **105**, 1–4 (2010).

8. Forslund, D. W., Kindel, J. & Mori, W. Two-Dimensional Simulations of Single-Frequency and Beat-Wave Laser-Plasma Heating. *Physical Review Letters* **1**, (1985).

9. Sakharov, A. & Kirsanov, V. Theory of Raman Scattering for a Short Ultrastrong Laser Pulse in a Rarefied Plasma. *Physical Review E* **49**, (1994).

Relativistic Raman Side Scatter Measurements in a Laser Wakefield Accelerator

Contact *j.cole11@imperial.ac.uk*

J. M. Cole, M. S. Bloom, M. J. V. Streeter, A. Dangor, S. P. D. Mangles, Z. Najmudin

The John Adams Institute for Accelerator Science,Blackett Laboratory, Imperial College London, SW7 2AZ, UK

J. Holloway, S. Mandry

High Energy Physics Group, University College London, WC1E 6BT, UK

D. R. Symes, K. Poder, O. Chekhlov, S. J. Hawkes

Central Laser Facility, STFC Rutherford Appleton Laboratory, Chilton, Didcot, OX11 0QX, UK

Introduction

The long-term future of high-energy particle accelerators would benefit from new, scalable accelerator technology. One such plasma-based approach is Laser Wakefield Acceleration (LWFA)[1–3], currently capable of the acceleration of electrons to energies of 2GeV[4]. The ability of plasmas to support very high electric fields confines the acceleration length to several centimetres, rather than the many metres required in conventional radio frequency-based linear accelerators.

Before an electron beam can reach these high energies, the drive laser must establish a high-amplitude plasma electron density wave. The coupled evolution of the laser pulse and plasma wave is a highly nonlinear process, and is sensitive to the bulk plasma parameters. A major contributor to the qualitative long-term behaviour of the plasma wave is the electron density. Above a certain threshold the plasma becomes dense enough that the laser pulse can self-guide, extending the acceleration length. The next density threshold is that for self-injection, where the wakefield becomes strong enough to trap stationary electrons from the background plasma. Knowing the average plasma density is then critical to understanding the regime of operation of the accelerator.

In this report we compare two common electron density diagnostics – direct high-magnification Mach-Zehnder interferometry, and Raman side-scatter spectroscopy. The two are found to agree if the relativistic motion of the plasma electrons is taken into account. The experimental data comes from a LWFA experiment performed with the ASTRA laser delivered to Target Area 2.

Experimental Setup

Figure 1 shows a simplified schematic of the layout of the TA2 vacuum chamber – optics for additional diagnostics aren't indicated. The 60mm diameter, 800nm wavelength ASTRA beam was focused with a 1 metre focal length (f/16) off-axis parabolic mirror to a slightly elliptical spot of FWHM 19×22μm with a Rayleigh range of 540μm. Approximately 35% of the pulse energy was contained within the FWHM ellipse as calculated from a calibrated image of the focal spot. With a measured pulse length of 37-45fs and shot-to-shot variation in energy of 600-650mJ, the peak focal spot intensity was 2.1-2.8×10^{18}Wcm^{-2} corresponding to a normalised vector potential (in vacuum) of $a_0 = eE_0/m_e c\omega_0$ = 1.0 - 1.2.

The probe beam and main beam are split through a bemsplitter after the second amplifier, with the probe beam compressed in a separate grating compressor in TA2 outside vacuum. The probe was spectrally broadened through self-phase modulation in a noble-gas-filled hollow-core fibre and finally recompressed with a set of chirped mirrors[5]. The probe pulse length was measured to be 15-25fs FWHM, which combined with its clean 5mm-diameter beam profile supported clear interferometry and shadowgraphy of the plasma channel. The pulse length varied day-to-day and signifies the difficulty in achieving such short pulses. The polarisations of the two beams were crossed and a polariser was inserted between the interaction and the transverse imaging diagnostics. In this way the amount of pump light scattered into the diagnostics could be lowered. A probe delay stage was mounted on a μm-precision delay stage allowing fine control of the relative beam timing.

The self-injection threshold[6] for the ASTRA laser bounds $n_e >$ 1.5×10^{19}cm^{-3}, leading to a dephasing length $\lambda_d = \lambda_p n_c/n_e <$ 1mm. Accounting for the distance required for pulse evolution the target was chosen to be a 2mm diameter supersonic gas nozzle. Helium gas at up to 50bar was delivered through a Parker solenoid valve, reaching electron densities of 1×10^{20}cm^{-3}. The typical neutral-gas density profile of the jet was trapezoidal, with 150μm-long linear ramps at the edges leading to a constant-density plateau.

The electron spectrometer comprised of a 0.7T 10cm permanent magnet and a scintillating LANEX screen. High-energy electrons were dispersed across the screen, and the scintillation light was imaged into a 14-bit filtered camera. The measurement range of the spectrometer was 10-70MeV, and typical peak electron beam energies were near 50MeV. A second LANEX screen could be inserted before the magnet to characterise the beam size and pointing stability, which were approximately 10mrad and 30mrad RMS respectively.

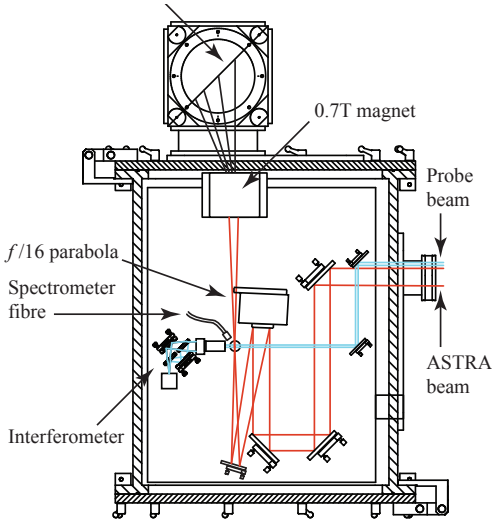

Figure 1: Vacuum chamber layout with relevant diagnostics highlighted

Raman Side Scatter

The peak laser intensities required for effective LWFA are sufficiently high ($>10^{18}$Wcm^{-2}) that plasma electrons are accelerated to relativistic velocities in a single optical cycle. This is also far above the level where one would expect nonlinear optical processes to take place. Raman Side Scatter (RSS) is a process where a pump wave ω_0 scatters from a plasma electron wave ω_p. In the process a new plasma wave with frequency approximately ω_p is generated in the transverse direction. The scattered light ω_s leaves the plasma in the forward direction, but at an angle to the incident pump wave defined by k-matching[7]. Conserving energy throughout the scattering process we have $\omega_0 = \omega_p + \omega_s$, showing that the scattered light is downshifted from the pump by the plasma frequency. By measuring the spectrum of the light leaving the plasma in the side direction it is then possible to measure the frequency of the electron wave. For a scattered wave satisfying $k\lambda_D << 1$ in background electron density n_e this is given by $\omega_p = (n_e e^2/m_e\varepsilon_0)^{1/2}$, and the average electron density in the plasma channel can be recovered.

In this experiment a spectrometer fibre was fixed pointing at the gas jet to collect the scattered light, and passed out of the chamber with a vacuum feedthrough. The fibre was positioned directly above the gas jet at an angle close to 90° with a collection lens attached to sample light from the entire gas jet. An Ocean Optics HR2000 spectrometer recorded the spectrum on every shot.

Mach-Zehnder Interferometry

A more direct measurement of the plasma density is through interferometry. Here a probe beam is passed through the plasma and the phase shift of the beam is measured. The phase shift is proportional to the chord-integrated electron density, but if the plasma is assumed to be cylindrically symmetric the projected phase shift can be Abel-inverted to obtain the density everywhere in the plasma.

In this experiment the interferometry took place completely inside the vacuum chamber to minimise any imaging aberrations caused by vacuum windows. In addition a high-quality 10x magnification microscope objective (Mitutoyo M-Plan APO NIR 378-823-5) and tube lens (Mitutoyo MT-L4) were used to ensure high imaging quality across the field of view of the camera. The interferometer was designed in such a way that one of the arms was completely reflective – this was the arm used to form an image on the CCD. The second arm was used to offset the image vertically to act as a reference for the interferometry. When assembled, the entire diagnostic fitted onto a small 175×225mm breadboard inside the chamber, which was then mounted on a 3-axis stage.

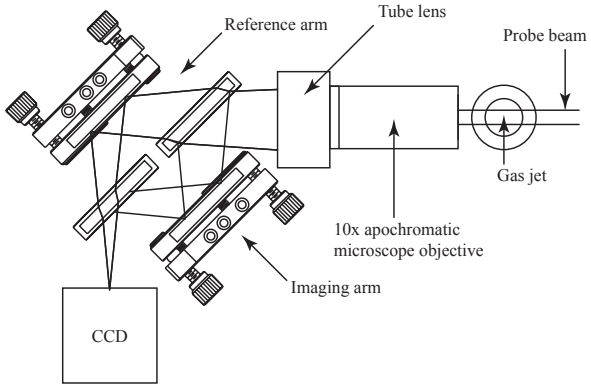

Figure 2: Interferometry layout

Due to the high magnification, our field of view was limited to 280μm so the interferometer stage was motorised along the pump laser propagation axis. Simultaneous adjustments of the probe timing and interferometer position allowed probing of the entire length of the gas jet. The depth of focus of the microscope objective was 4μm, so before acquiring an image the interferometer was manually focused onto small structures on an alignment wire. The flexibility of the Mach-Zehnder arrangement allows independent control of the fringe spacing – smaller fringes support higher spatial resolution at the expense of lower phase resolution due to the lower number of pixels per fringe. In this experiment the phase resolution was 0.1π.

An example interferogram is plotted in Fig. 3 alongside the retrieved phase shift. The ultrashort nature of the probe pulse caused the fringe visibility to vary significantly over the field of view of the camera. To alleviate this an 820±5nm bandpass filter was placed in front of the CCD. This lengthens the pulse enough to restore high-visibility fringes, but doesn't affect the imaging quality.

The majority of the self-emission was eliminated with a high-extinction-ratio polariser placed in front of the CCD, as the scattered light was the same polarisation as the pump beam. The small amount visible at high densities indicated the time-integrated history of the pump beam path, where occasionally at high densities some hosing was evident.

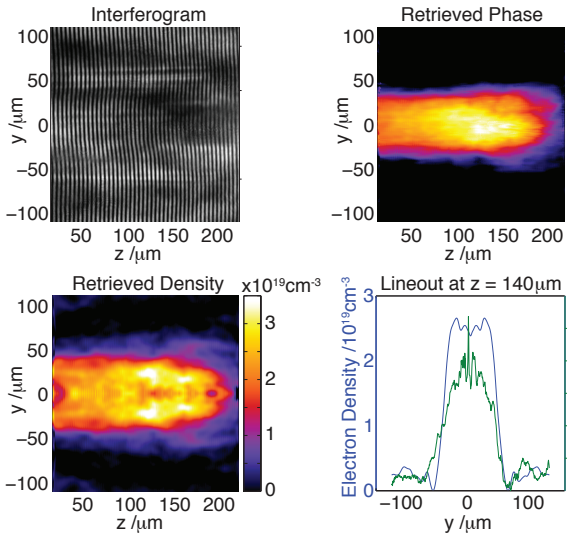

Figure 3: An example interferogram with its associated phase and density retrievals

The probe imaging was detailed enough to resolve fine filamentary structures in the channel, as well as the large-scale features. We often saw a central denser plasma channel, surrounded by a less dense halo. When taking an average density measurement the central dense portion is used, averaged over a 10μm diameter cylinder, as this is the region of the laser-plasma interaction. The plasma wavelength at 10^{19}cm^{-3} is approximately 10μm, which 3D simulation and theory predicts to be the transverse size of the wakefield[8].

The phase retrieval was performed with a Hilbert-transform-based method which is markedly less noisy than FFT-based methods, while being an order of magnitude quicker than Continuous Wavelet Transformation (CWT)-based decompositions[9]. In this way several hundreds of interferograms may be analysed in an afternoon. Using this method a linear fit was found between the central channel plasma density and the gas jet backing pressure.

Comparison of RSS Spectra With Interferometry

A typical run of shots in this experiment was a plasma density scan. This was achieved in practice by filling the gas jet reservoir to a high pressure, then taking shots while the gas jet backing pressure is allowed to fall down to zero. This method

has the advantage that the fractional change in density between shots stays roughly constant throughout the scan. For a particular run of 104 shots analysed here, the gas jet pressure was varied from 23bar down to 0.1bar with RSS spectra recorded on every shot. Fig. 4 collates the spectra together so that trends may be observed more easily.

Immediately obvious is the scattered peak of the pump beam centred near 810nm with a FWHM of approximately 40nm. The height of this peak stays very similar throughout the density scan suggesting this is laser reflection from the gas jet or surrounding structures, rather than from the plasma. At higher densities we begin to see significant amounts of $\lambda < 800$nm light, most likely due to ionisation blueshift.

The Raman signal is clearly visible as a series of increasingly bright peaks which gradually move higher in wavelength as the backing pressure grows. The blue circles in the figure mark the peaks of the spectra above 830nm to help identify the location of the RSS.

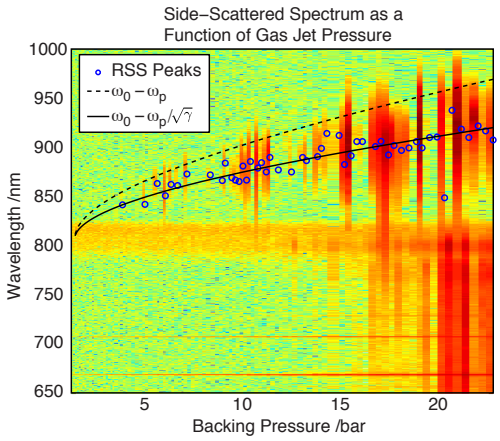

Figure 4: Side-scattered spectra recorded during a density scan. No data has been excluded, the colour scale is logarithmic

The dashed line shows the expected RSS peak ($\omega_0 - \omega_p$), based on an independent interferometric measurement of the plasma density – no fitting was performed for the plot. The final factor to take into account is the relativistic motion of the electrons in the plasma wave. When oscillating in a linearly-polarised laser field of strength a_0 an electron will attain an effective peak Lorentz factor of $\gamma = 1 + a_0^2/2$. The plasma frequency is then relativstically lowered to $\omega_p/\sqrt{\gamma}$, and this is plotted as the solid line in Fig. 4. The fact that the relativistic modification is required to fit the interferometry data suggests that the RSS originates from the region of the plasma near the pump pulse. However, the fact that it is the peak γ factor rather than the time averaged $\langle\gamma\rangle = 1 + a_0^2/4$ that is important is unexpected. The γ value is also calculated from the expected vacuum intensity, but in the plasma densities considered here it would be expected that the pulse would quickly self-focus down to a matched spot size $\approx \lambda_p/2$, significantly boosting a_0 beyond its vacuum value. In similar experiments on the ASTRA and Gemini lasers the plasma self-emission and RSS is seen to occur at the beginning of the plasma channel as the laser begins to self-focus. The shifts we see here are only consistent with the interferometric density measurements if a_0 is taken to be near its vacuum value, suggesting the majority of the RSS occurs at the beginning of the region of peak plasma density but well before the laser has self-focused.

In the linear regime the Raman scattering instability has a growth rate[10] $\Gamma = a_0(\omega_0\omega_p/8)^{1/2}$ at 90° and so the expected FWHM bandwidth of the RSS peak is $2\Gamma \propto \omega_p^{1/2}$. For $a_0 \to 1$, the strongly-driven RSS regime, the growth rate is also proportional to the plasma frequency when the scattered wave is resonant, i.e. when $(\omega_0 - \omega_p)^2 = \omega_p^2 + (\boldsymbol{k}_0 - \boldsymbol{k}_p)^2c^2$. Though not plotted for simplicity, the bandwidth increases with plasma density and agrees qualitatively with the spectra in Fig. 4.

Conclusions

Spectroscopy of scattered light from a LWFA has been shown to be an effective measurement of the plasma electron density in the region where electrons are injected and accelerated, assuming the laser intensity is known. The frequency downshifting of the scattered light agrees well with independent interferometry, but only if relativistic motion of electrons is taken into account. Alignment of the spectrometer fibre is trivial, and very little room is taken up in the often cramped target chamber. Though interferometry provides significantly more detailed information about the structure of the plasma channel, it is a more difficult diagnostic to implement, especially for ultrashort probe pulses. Analysing interferometry on-shot is challenging, limited primarily by computation time in a high-repetition-rate experiment on ASTRA. RSS spectroscopy allows immediate feedback on plasma density, simplifying the commissioning and monitoring of a LWFA experiment.

Acknowledgements

The authors would like to thank the CLF staff running the laser and assisting in the target area, and those proving technical support throughout the experiment.

References

1. Mangles, S. P. D. *et al*. Monoenergetic beams of relativistic electrons from intense laser-plasma interactions. *Nature* **431**, 535–538 (2004).

2. Faure, J. *et al*. A laser-plasma accelerator producing monoenergetic electron beams. *Nature* **431**, 541–544 (2004).

3. Geddes, C. G. R. *et al*. High-quality electron beams from a laser wakefield accelerator using plasma-channel guiding. *Nature* **431**, 538–541 (2004).

4. Wang, X. *et al*. Quasi-monoenergetic laser-plasma acceleration of electrons to 2GeV. *Nature Communications* **4**, (2013).

5. Nisoli, M., De Silvestri, S. & Svelto, O. Generation of high energy 10 fs pulses by a new pulse compression technique. *Applied Physics Letters* **68**, 2793 (1996).

6. Mangles, S. P. D. *et al*. The self-injection threshold in laser wakefield accelerators. *Physical Review Special Topics - Accelerators and Beams* 2–7 (2011).

7. Forslund, D. W., Kindel, J. & Mori, W. Two-Dimensional Simulations of Single-Frequency and Beat-Wave Laser-Plasma Heating. *Physical Review Letters* **1**, (1985).

8. Lu, W. *et al*. A nonlinear theory for multidimensional relativistic plasma wave wakefields. *Physics of Plasmas* **13**, 056709 (2006).

9. Tomassini, P. *et al*. Analyzing laser plasma interferograms with a continuous wavelet transform ridge extraction technique: the method. *Applied optics* **40**, 6561–8 (2001).

10. Kruer, W. *The Physics of Laser Plasma Interactions*. (2003).

High Energy, High Charge Electrons and Energetic X-rays from a Density Tailored Gas Target

Contact *jonathan.wood08@imperial.ac.uk*

J. C. Wood

The John Adams Institute for Accelerator Science, Blackett Laboratory, Imperial College London, SW7 2AZ, UK

J. M. Cole, A. E. Dangor, N. P. Dover, S. Kneip, S. P. D. Mangles, H. Nakamura, K. Poder, M. J. V. Streeter, Z. Najmudin

The John Adams Institute for Accelerator Science, Blackett Laboratory, Imperial College London, SW7 2AZ, UK

N. Booth, D. R. Symes

Central Laser Facility, STFC Rutherford Appleton Laboratory, Chilton, Didcot, OX11 0QX, UK

N. C. Lopes

GoLP/Centro de Fisica dos Plasmas, Instituto Superior Tecnico, Lisboa, Portugal and The John Adams Institute for Accelerator Science, Blackett Laboratory, Imperial College London, SW7 2AZ, UK

S. Hillenbrand

CERN, Geneva, Switzerland and KIT, Karlsruhe, Germany

J. Osterhoff, C. A. J. Palmer, L. Schaper

DESY, Hamburg, Germany and Plasma Accelerator Group, University of Hamburg, 20148 Hamburg, Germany

Introduction

Since it was first proposed in 1979 [1] laser wakefield acceleration (LWFA), the technique of accelerating electrons in the plasma wave left in the wake of a high intensity laser pulse, has been very attractive due to the extremely high accelerating gradients that a plasma can support (~100GV/m). Therefore this has been a very active research area. Electron bunches with an energy spread of a few percent have been produced [2] [3] [4], and energies up to [5] [6] and beyond [7] 1 GeV have been observed from centimetre-scale plasmas. An important feature is the production of high brightness, temporally short x-ray beams that could find application in university or medical labs, in which they would easily fit thanks to the small footprint of a laser wakefield accelerator.

This report focuses on data from a 3-compartment gas cell target with a density step/ down-ramp between the second and third compartments. Controlling the size of this dip allowed the maximum electron energy and total accelerated charge to be tuned. As the pressure in the third compartment was decreased a rapid increase in the energy of the x-ray beam was observed, with maximum critical energies of approximately 18 keV.

Betatron Radiation from Laser Wakefield Accelerators

A LWFA can produce x-rays without an insertion device such as an undulator or a wiggler. In the nonlinear bubble regime [8] [9], the bubble itself acts as a wiggler because the space charge distribution provides a restoring force towards the central axis. Any electron injected into the bubble off axis will oscillate. This produces 'betatron radiation' [10] [11] [12]. The electron oscillates at the betatron frequency $\omega_\beta = \omega_p/\sqrt{(2\gamma)}$ where ω_p is the plasma frequency and γ is the Lorentz factor of the electron. This produces radiation in the lab frame at frequencies of order $\omega \approx 2\gamma^2\omega_\beta$, well within the x-ray region of the spectrum for electron energies greater than 100MeV. The shape of the frequency spectrum of this radiation depends upon the wiggler parameter $K=\gamma r_\beta \omega_\beta/c$ where r_β is the radius of the betatron oscillations [13]. For $K \ll 1$, the undulator regime, the radiation is narrowly peaked. In the wiggler limit ($K \gg 1$) the radiation is broadband. Its' on-axis intensity is described for a single electron by equation 1, where N_β is the number of oscillations the electron performs, $K_{2/3}$ is a modified Bessel function of the second kind and the critical energy $E_{crit} = 1.5\hbar K\gamma^2\omega_\beta$ is the energy above and below which half of the energy in the spectrum is contained. The radiation is in the forward direction in a cone with a half-angle of approximately K/γ.

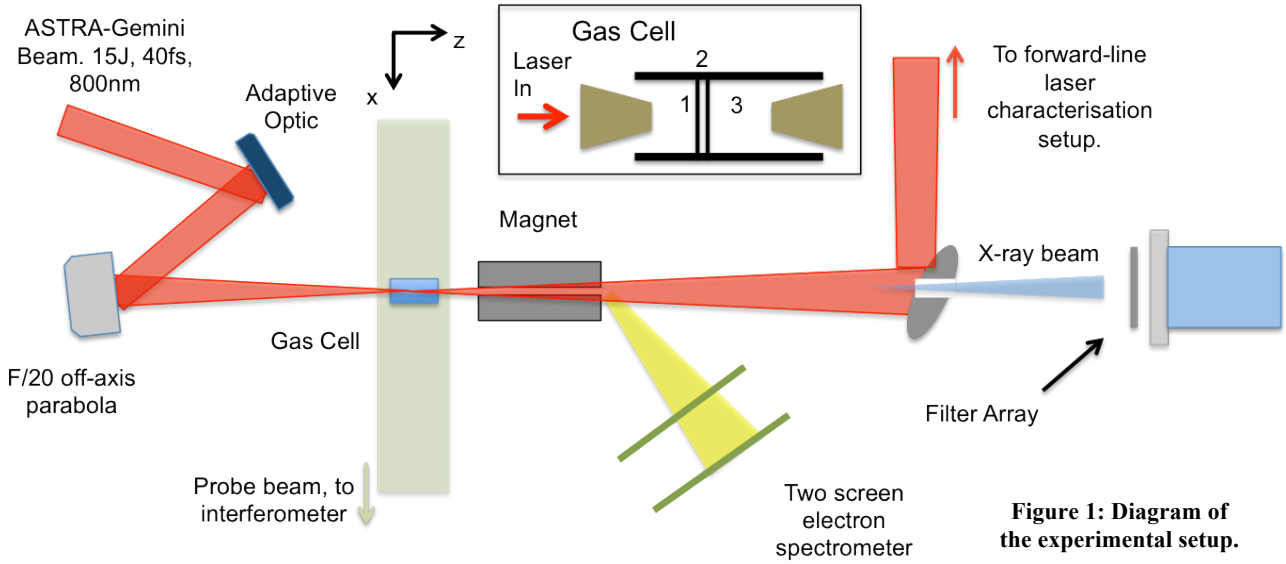

Figure 1: Diagram of the experimental setup.

$$\frac{d^2I}{dEd\Omega} \approx N_\beta \frac{3e^2}{2\pi^3\hbar c\epsilon_0}\gamma^2\left(\frac{E}{2E_{crit}}\right)^2 \mathcal{K}_{2/3}^2(E/2E_{crit}) \quad (1)$$

Experiments have observed critical energies of many keV [14] [15] [16], peak brightnesses of 10^{17}-10^{19} photons/s/mm^2/mrad^2 /0.1% BW [14] [15]. Kneip *et al*. later increased the brightness by 3 orders of magnitude by operating in a more strongly nonlinear regime [13]. Source sizes as small as 2-3μm have been reported [13] [17].

Experimental Setup

The experiment detailed was a laser wakefield accelerator experiment conducted using the Astra-Gemini Laser (15J, 40fs). A diagram of the setup is shown in figure 1. The target was a three-compartment gas cell (inlaid in figure 1). The 3 compartments allowed for a number of different density profiles to be created because the pressure of each could be controlled separately. In practice only two gas lines were available so often two compartments were held at the same pressure, as the compartments could be linked. The effective length of the gas cell could be altered by moving the metal cones through which the laser entered and exited. The magnet dispersed electrons according to their momentum on to two scintillating Lanex screens, acting as an electron energy spectrometer.

Characterising the X-ray Spectrum

The critical energy (E_{crit}) of the x-rays was estimated by imaging an array of thin metal filters with an Andor Ixon-M DD x-ray camera. The quantum efficiency data for this camera was only available for photon energies up to 20 keV. Cutting off the camera response function at this energy would have lead to an under-estimation of the critical energy. Higher photon energies were accounted for by extending the data provided by Andor using the silicon absorption curve from the NIST database [18].

Figure 2 shows an example image of the filter array [19] illuminated by a LWFA produced x-ray beam. The filter array was assembled on top of two layers of aluminised mylar and was shielded by a further layers of aluminium to protect it from the laser. There are 14 filters plus two blanks in the array, made of 10 different materials. The repeated materials are useful to quantify the variations in the x-ray spectrum across the field of view. Each different material has a different curve describing its' x-ray transmission as a function of energy. The transmission curves could be drastically different between two different materials in the x-ray regime due to the presence of K_α edges. Materials are very transmissive up to their K_α edges and absorb strongly at and above them. This is a very useful feature when characterising x-ray energies because one can confidently extract a lot of spectral information by comparing the number of photons transmitted through each filter.

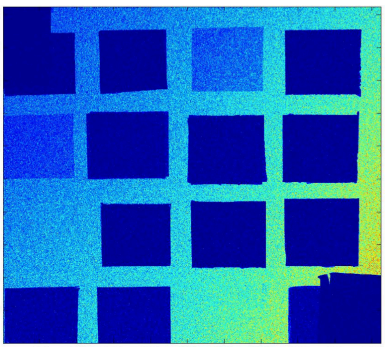

Figure 2: Example image of the filter array illuminated by a LWFA produced x-ray beam.

The shape of the x-ray energy spectrum was assumed to be an on-axis synchrotron spectrum described by equation 1. This approximation appeared to fit the results well. The estimated number of photons transmitted through each filter (i), $N^i_{guess}(E_{crit})$, was calculated from this spectrum across a range of critical energy values using equation 2. Q is the quantum efficiency of the camera, T is the transmission function of the filter material and S is the x-ray energy spectrum.

$$N^i_{guess} \propto \int_0^{Emax} E.Q(E)T(E)S(E,E_{crit})dE \quad (2)$$

N^i_{guess} was compared to the number of counts observed on each filter N^i_{data}. So that the comparison could be done for a single parameter only (E_{crit}), the estimated and actual number of counts on each filter were normalised so that the average number of counts per filter was 1. The critical energy was estimated by minimising the quantity $(N^i_{guess} - N^i_{data})^2$ summed over every filter.

Electron Data

The results in this section were taken with the total length of the gas cell set to 10mm. There was an equal backing pressure of the first and second compartments of the cell, *P1*, which was held constant at 300mbar. The pressure in the third compartment, *P2*, was varied between 125mbar and 300mbar, which changed the size of the density dip in the plasma density profile.

Typically the electron energy spectra $dN/(dE/E)$ produced under these conditions had one or more quasi-monoenergetic peaks at high energy followed by a long 'tail'. An example of this is shown in figure 3. Typically features like this are indicative of injection occurring in multiple bunches.

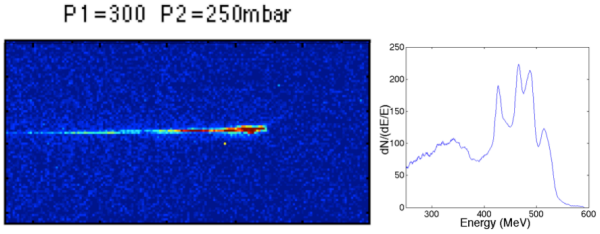

Figure 3: Left: example image of the first electron spectrometer screen. The energy dispersion direction is horizontal with the highest energy electrons towards the right hand side. Right: plot of the energy spectrum $dN/(dE/E)$ vs. E for this shot.

The maximum energy at which electrons were observed and the total accelerated charge are plotted against *P2* in figure 4. The error bars indicate the standard error calculated from the variance from multiple shots. There is a clear variation in maximum electron energy with *P2* and there is an indication that there is an optimal and least optimal magnitude of the density dip (*P1*-*P2*).

The total accelerated charge also varies strongly with *P2*. Comparing the data at *P2*~160mbar and *P2*~275mbar the total charge is similar but the electron energy is considerably higher at *P2*~160mbar. This suggests that having a suitably large dip in the density profile is a good method of accelerating a high charge to high energy.

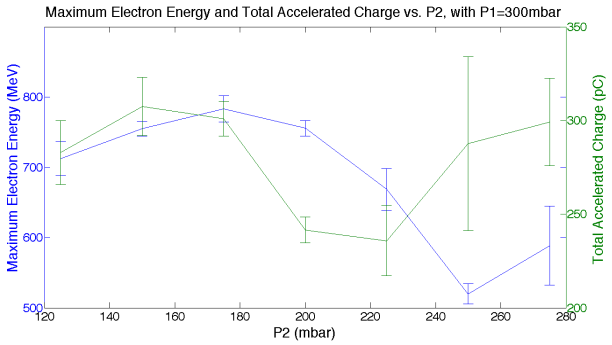

Figure 4: Maximum recorded electron energy (blue) and total accelerated charge (green) for 10 mm and 15 mm gas cell lengths plotted against the backing pressure of the second compartment of the gas cell (*P2*). The backing pressure of the other compartments (*P1*) was 300 mbar.

X-ray Critical Energy

Figure 5 shows the x-ray critical energy E_{crit} as a function of *P2*. This data is from the same shots as the electron data shown in figure 4. E_{crit} is highest for low *P2*. The maximum electron energies are high at low *P2*, which increases the critical energy because E_{crit} is proportional to the γ^2 factor of the electrons. In addition to this, in the lower density region the radius of the betatron oscillations, r_β, is increased. This is because the restoring force due to the space charge in the bubble is smaller at lower number densities. E_{crit} is linearly proportional to r_β so it is increased via this method, similar to a proposal by Ta Phuoc [20]. This is a convenient method of producing higher energy x-rays without increasing the laser energy.

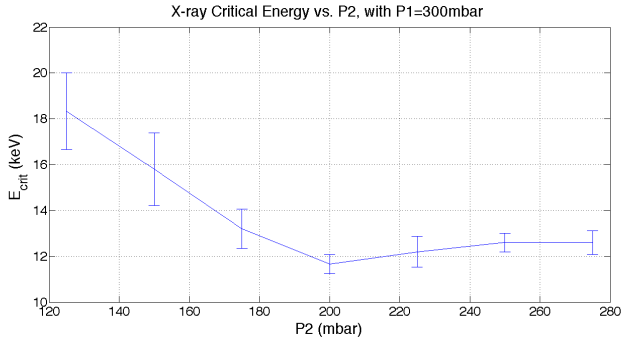

Figure 5: X-ray critical energy vs. P2.

Conclusions

In this report it has been demonstrated that the amount of charge and the energy of a LWFA produced electron bunch can be tuned by controlling the plasma density profile, specifically by incorporating a density step/ down-ramp in the plasma profile. For large dips a significant enhancement of the critical energy of the betatron emission was observed, rising to approximately 18 keV.

Acknowledgements

This work was funded by The John Adams Institute, EPSRC and grant number EP/H00601X/1. We thank the engineering staff at the CLF for their invaluable assistance.

References

1. T. Tajima and J.M. Dawson. PRL, 4(4):267– 270, 1979.
2. SPD Mangles et al. Nature, 431:535–538, 2004.
3. CGR Geddes et al. Nature, 431:538–541, 2004.
4. J. Faure et al. Nature, 431:541–544, 2004.
5. K. Nakamura et al. Physics of Plasmas, 14(5):056708, 2007.
6. W. P. Leemans et al. Nature Physics, 2(10):696–699, September 2006.
7. X. Wang et al. Nature Comms., 4(1988), June 2013.
8. A. Pukhov and J. Meyer-ter Vehn.. Applied Physics B: Lasers and Optics, 74(4-5):355–361, April 2002.
9. W. Lu et al. PRL 96(16):165002, April 2006.
10. E. Esarey et al. Phys. Rev. E, 65(5):056505, May 2002.
11. I. Kostyukov et al. Physics of Plasmas, 10(12):4818, 2003.
12. I. Kostyukov et al. Physics of Plasmas, 11(11):5256, 2004.
13. S. Kneip et al. Nature Phys., 6(12):980–983, October 2010.
14. A. Rousse et al. PRL, 93(13):1–4, September 2004.
15. S. Kneip et al. PRL, 100(10):105006, March 2008.
16. S Fourmaux et al. New Journal of Physics, 13(3):033017, March 2011.
17. F. Albert et al. Plasma Physics and Controlled Fusion, 50(12): 124008, December 2008.
18. J.H. Hubbell and S.M. Seltzer. Online at http://www.nist.gov/pml/data/xraycoef/ 2011.
19. Designed by M. Bloom at Imperial College London.
20. K. Ta Phuoc et al. Physics of Plasmas, 15(6):063102, 2008.

Thorough Calibration of a Scintillating Lanex Screen as an Electron Bunch Charge Diagnostic

Contact *jonathan.wood08@imperial.ac.uk*

J. C. Wood
The John Adams Institute for Accelerator Science, Blackett Laboratory, Imperial College London, SW7 2AZ, UK

J. M. Cole, A. E. Dangor, N. P. Dover, S. Kneip, S. P. D. Mangles, H. Nakamura, K. Poder, M. J. V. Streeter, Z. Najmudin
The John Adams Institute for Accelerator Science, Blackett Laboratory, Imperial College London, SW7 2AZ, UK

N. Booth, D. R. Symes
Central Laser Facility, STFC Rutherford Appleton Laboratory, Chilton, Didcot, OX11 0QX, UK

N. C. Lopes
GoLP/Centro de Fisica dos Plasmas, Instituto Superior Tecnico, Lisboa, Portugal and The John Adams Institute for Accelerator Science, Blackett Laboratory, Imperial College London, SW7 2AZ, UK

S. Hillenbrand
CERN, Geneva, Switzerland and KIT, Karlsruhe, Germany

J. Osterhoff, C. A. J. Palmer, L. Schaper
DESY, Hamburg, Germany and Plasma Accelerator Group, University of Hamburg, 20148 Hamburg, Germany

Introduction

An important characteristic of any particle accelerator is the total charge of the accelerated bunch that they output. In laser wakefield acceleration experiments, this is often calculated from images taken of a scintillating Lanex screen with a CCD camera. Therefore it is necessary to know how many electrons are required to produce a single count on the greyscale camera image. Lanex response as a function of charge is well known [1]. However the transmission of light through the optics to the camera, and the response of the camera, are not always well characterised. This report presents a method whereby the image of the scintillator is compared to an image plate reading of the same shot. A number of important considerations, including the modified response of Lanex and image plate at GeV electron energies, geometrical factors, natural decay of image plate signal and possible saturation effects are described in detailing the method for this charge calibration.

Experimental Setup

The experiment detailed was a laser wakefield accelerator experiment conducted using the Astra Gemini Laser, producing electrons with energies on the order of 1GeV. A two-screen electron spectrometer was deployed to measure the electron energies, as in figure 1. Shown in this figure are the image plate positions for the single shot on which the calibration was performed. The scintillating screens used, angled at 45° to the vertical, were Kodak Lanex Regular, and the image plate was Fujifilm BAS-MS.

Figure 1: Setup for the lanex screen

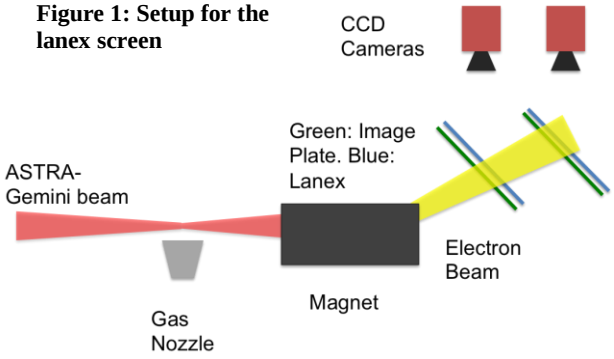

The image plate does not absorb any electrons at the energies observed in the experiment, but the electrons produce a phosphorescent response from the image plate. The magnitude of this response can be used to find the charge on that shot, as will be described in the coming sections, and a comparison to the image of the Lanex on the shot allows for a calibration to be made. In order to build up a method for the calibration, the properties of lanex and image plate must first be discussed.

Properties of Lanex

Lanex is a Gadolinium oxysulphide (Gd_2O_2S:Tb) based fluorescent scintillator that is used to detect ionising radiation. After exposure to ionising radiation the active compound in the Lanex de-excites on the millisecond timescale emitting light with a wavelength of approximately 545nm [2]. Such scintillating screens are ideal for reasonably high-rep rate experiments as they provide suitable resolution, are relatively inexpensive and are not single-shot detectors like image plate. Nakamura et al. [3] concluded that the number of photons emitted by the Lanex is linearly proportional to the charge of the electron beam that passes through it at constant energy. Buck et al. [1] found the same for charges in the range of 1 pC to 20,000 pC using picosecond electron bunches.

Properties of Image Plate

Image plate works on the principle of phosphorescence. A dopant material (Eu^{2+} in this case) is excited to a metastable state by absorption of x-ray radiation or interaction with a charged particle [4]. These metastable states naturally decay emitting a photon, but this decay can also be stimulated with a light source. An image plate scanner illuminates the image plate with a laser and records the number of emitted photons with a photomultiplier tube (PMT). By scanning across the whole image plate in this way, a map of how much radiation detected in each region is built up. Image plate is sensitive across many orders of magnitude of dose. To account for this and produce a reasonable image, the scanner software employs a logarithmic data amplifier. The actual photo-luminescent signal that the PMT in the scanner measures (*PSL*) is related to the scanner output signal ('Quantum Level' or *QL*) by equation 1. *R* is the scanner resolution in microns, *S* is a quantity called sensitivity which is equal to 5000 for the scanner used (FLA-5100), $L = 5$ for this scanner and *G* is the bit depth of the scan (65535 for the 16 bit scans performed here).

$$PSL = \left(\frac{R}{100}\right)^2 \left(\frac{4000}{S}\right) 10^{L\left(\frac{QL}{G}-\frac{1}{2}\right)} \quad (1)$$

1 *PSL* is equivalent to 50 electron counts in the electron energy range 1-100MeV for image plate type BAS-MS [4]. However there are a number of further properties of image plate that need to be taken into account when calculating how much charge each *PSL* count corresponds to. These are listed in the next section along with a number of experimental factors that also affected this figure.

Factors Affecting the Method of Calibration

Energy dependence of Image Plate and Lanex signal: There is a 1% decrease in the number of photons emitted by lanex for every 100MeV increase in electron energy between 106 and 1522MeV.

For image plate Tanaka et.al. [5] and Nakanii et al. [6] explored this issue. They used image plate type BAS-SR rather than BAS-MS, but the composition of each is quite similar [7], so it was assumed that the energy dependence of each is similar. A graph of PSL per electron versus electron energy taken from their paper is shown in figure 2. There is a notably higher response below 1 MeV but that is of no concern for this calibration. At high energy there is a considerable variation in the sensitivity that must be taken into account.

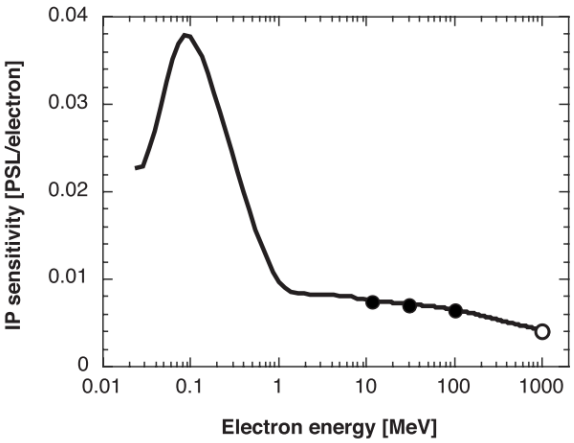

Figure 2: Variation of the Sensitivity of Imaging Plate with Electron Energy [6].

Assuming a zero divergence electron beam exiting the plasma on and parallel to the laser axis, the position of an electron on the Lanex screen and the image plate is uniquely determined by its' energy because of the magnetic field. The sensitivity of the image plate and the Lanex was determined at every position on both detectors using the above information, and the signal corrected for at that position.

Geometrical Factors: Lanex is a Lambertian emitter [1] meaning that the observed number of Lanex counts will vary cosinusoidally with the angle at which the camera is placed, with maximum emission perpendicular to the Lanex surface. This is just a simple geometrical factor, of $1/\sqrt{2}$ in this case, which we do not need to account for because we are calibrating the signal seen on the camera with the number of electrons from the image plate.

Secondly, because the Lanex and the image plate was angled at 45° to the vertical, electrons travelling on different trajectories will interact with different thicknesses of each, as demonstrated in figure 3. The trajectories were assumed to be straight lines coming from the magnet centre. The path length δx through a piece of image plate, thickness δx, of an electron travelling at angle θ upwards from the horizontal is given by equation 2.

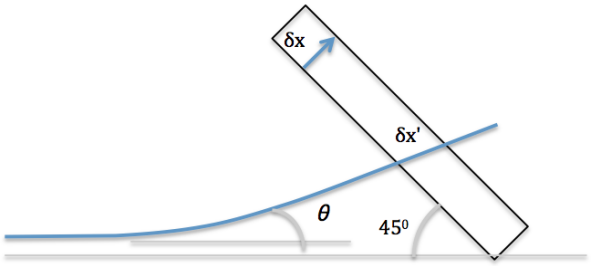

Figure 3: Electrons travelling on different trajectories interact with different thicknesses of the active compound in the image plate and the Lanex.

$$\delta x' = \frac{\delta x}{cos(45-\theta)} \quad (2)$$

The signal at any one point will be 'geometrically amplified' by this factor, which was corrected for each point, as was done for the energy sensitivity. In addition, angling the Lanex at 45° meant that the bottom of the Lanex screen was further away from the camera than the top, which means that one pixel on the camera corresponded to a different length of Lanex. Rulers placed alongside the Lanex screen allowed this variation to be quantified and a polynomial was fitted to this data to give the distance along the Lanex screen as a function of camera pixel.

Natural decay of PSL signal with time: *PSL* counts recorded by image plate of type BAS-MS naturally decay slowly with time. During the 20-minute wait between the interaction and scanning of the plate, the signal decayed to 92% of its initial magnitude. This has been quantified by Zeil et al. [8].

Materials placed in front of the Image Plate and Lanex: The image plate was wrapped in aluminium foil to protect it from light after the exposure because this causes the image plate signal to decay. The electron energies recorded on the image plate were over 200MeV, so it was assumed that the electrons would lose no energy in the foil. Image plate does scatter electrons of this energy, but will not absorb them meaning that the charge recorded by the Lanex should be the same as passed through the image plate.

Saturation of the Image Plate: The *QL* has a limit of 65535 for 16 bit scans meaning that, from equation 1, any *PSL* value above 253 per pixel (for 100um resolution) cannot be mapped to a large enough *QL* value. This problem of saturation was avoided by reducing the PMT voltage down to 400V from 800V. A comparison between signal levels at the two different voltages was done, although this could be a source of systematic error in this analysis that is not currently be corrected for.

Calibration Result

To take into account the factors outlined in the previous section a charge calibration matrix was produced that contained the charge per Lanex count for each camera pixel. In fact a vector would have sufficed; the geometrical and energy dependence factors vary only along the electron energy dispersion direction. However a matrix was more convenient as it allowed any Lanex image to be multiplied piecewise with the calibration matrix to convert the image from 'camera counts' to a 2D map of the

charge distribution. At low energy, a single count on the Lanex image was found to correspond to 3.30×10^{5} pC. For a typical shot the total charge of the accelerated electron bunch was at the 100 pC level. The chief systematic errors affecting the result both relate to the image plate scanners. The comparison of scans done with a PMT voltage of 400 V and 800 V should be improved: this should be done by delivering a known dose to two pieces of image plate, low enough to avoid saturation at both voltages, and then comparing the PSL counts on each. This method at 800 V would also allow the conversion factor of 50 electrons per PSL to be verified, the other potential source of significant systematic error.

Conclusions

This report detailed a method of calibrating a scintillating screen (Lanex) so that it could be used as an accurate diagnostic of the charge of an electron bunch that passes through it. The method involved placing image plate in front of the Lanex, and using the known properties of image plate to estimate the electron bunch charge. This was compared to the image of the Lanex screen. A number of factors including the energy sensitivity of Lanex and image plate, geometrical factors, the natural decay of image plate signal and the effects of image plate saturation were detailed so that they could be accounted for.

Acknowledgements

This work was funded by The John Adams Institute, EPSRC and grant number EP/H00601X/1. We thank the engineering staff at the CLF for their invaluable assistance.

References

1. A. Buck et al., Rev. Sci. Instrum. 81(3), 033301, 2010.
2. A.G. Glendinning et al., Physics in Medicine and Biology, 46, 517, 2001.
3. K. Nakamura et al., PRST-AB, 14(6), 062801, 2011.
4. Stefan Kneip. Laser Plasma Accelerator and Wiggler. PhD thesis, Imperial College London, 2010.
5. K. A. Tanaka et al., Rev. Sci. Instrum., 76(1), 013507, 2005.
6. N. Nakanii et al., Rev. Sci. Instrum., 79(6), 066102, 2008.
7. T Bonnet et al., Response function of imaging plates to protons and alphas : experimental results and modelisation. Presentation, 2012.
8. K Zeil et al., Rev. Sci. Instrum., 81(1), 013307, 2010.

Generation of giant attosecond pulse from laser-driven relativistic electron sheets

Contact Wenjun.Ma@physik.uni-muenchen.de, joerg.schreiber@mpq.mpg.de

W.Ma, J.Bin, C. Kreuzer, J. Schreiber

Department of Physics, Ludwig-Maximilians-University, 80539 Munich, Germany

M. Yeung, S. Matthew, S. Cousens, Dromey, M. Zepf

Department of Physics and Astronomy, Queen's University Belfast, Belfast, BT7 1NN, UK

H. Wang, J. Meyer-ter-Vehn

Max-Planck-Institute for Quantum Optics, D-85748 Garching, Germany

P. S. Foster

Central Laser Facility, STFC Rutherford Appleton Laboratory, Chilton, Didcot, OX11 0QX, UK

Introduction

As one of the most significant achievements in the field of ultrafast optics over the past decade, attosecond pulses generated from laser-irradiated noble gases at intensities of 10^{14}~ 10^{15} W/cm^2 enabled the real-time observation of ultrafast electron behavior in molecules and solids. At higher laser intensity (I>10^{17} W/cm^2), high-order harmonic emission from solid-density-plasma surface[1-3] was demonstrated as high-intensity attosecond source owning to its low divergence and high conversion efficiency[4]. In these well-established two regimes, the oscillating driving field typically generates trains of attosecond pulses separated by half an optical cycle. Such pulse trains are unsuited to probing attosecond phenomena that are non-recovering on the timescale of a laser cycle. Techniques which efficiently produce isolated attosecond pulses are under active investigation[5].

Apart from the well-established mechanisms, instead of employing periodic nonlinear process in atoms or plasma, a flying relativistic electron sheet (FRES) could be an ideal producer of isolated attosecond pulse[6,7]. It was recently observed[8] that the wavelength and duration of a counter-propagating probe pulse could be significantly down-shifted via coherent Thomson backscattering from a FRES. Here we report the first experimental realization of another intriguing option[9] to generate isolated giant attosecond pulse from FRES without any additional beam. By irradiating a double layer target made of ultrathin foils with S-polarized high-intensity laser under oblique incidence, a FRES is firstly generated and then transversely kicked by the drive pulse reflected at the second foil. Such coherent transverse motion of the FRES results in a transverse sheet current of 1.5 MA/cm^2, which eventually produce a giant attosecond pulse with a peak electric field over 1 TV/m.

Experimental setup

The experiments were conducted at the Astra Gemini Laser Facility, STFC Rutherford Appleton Laboratory. 50 femtosecond Ti:Sappire laser with peak intensity of 2×10^{20}W/cm^2 was s-polarized to irradiate single-layer and double-layer targets at normal and oblique incidence. XUV radiation emitted in the laser propagation direction was detected by a multi-angle transmission grating spectrometer as shown in Figure 1. Ultrathin free-standing diamond-like carbon (DLC) foils with thickness between 4 nm to 20 nm were used as single-foil targets or assembled as double-foil targets.

The multi-angle spectrometer is composed of a 10,000 groove/mm SiN transmission grating and a 1,000 groove/mm gold transmission grating array. The SiN grating was set along the laser axis, 93 cm away from the targets after a vertical slit, covering a spectral range of 3 nm-40 nm. The gold grating array was positioned slightly above the SiN grating to cover a spectral range between 30nm and 180nm. From the off-axis gold grating in the array, spectra under 1.3° could be registered. After the gratings, radiation was converted to electron signal through a microchannel plate (MCP), producing visible light on a fluorescent screen, and recorded by a ANDOR charge-coupled device (CCD) camera.

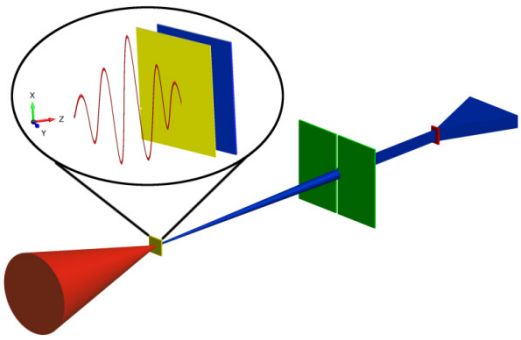

Figure 1. Experimental set-up. The double-layer targets were obliquely shoot by s-polarized laser pulse at intensity of 2×10^{20} W/cm^2. XUV radiation was detected by a multi-angle spectrometer after a vertical slit.

Experimental results

Figure 2 shows the measured spectra from 4 nm to 30 nm for different targets under different incidence angle. Intense continuum XUV radiation is observed exclusively for double layer targets under oblique incidence. This result follows theoretical prediction very well. The bandwidth of the continuum radiation is about 200 eV. It supports an isolated attosecond pulse with duration of the order of 100 as. On top of the continuum spectra, there is line emission from carbon and oxygen. The line emission for normal incidence and oblique incidence has the same magnitude of intensity, which indicates the increased signal under oblique incidence is not related to changes in the plasma parameters.

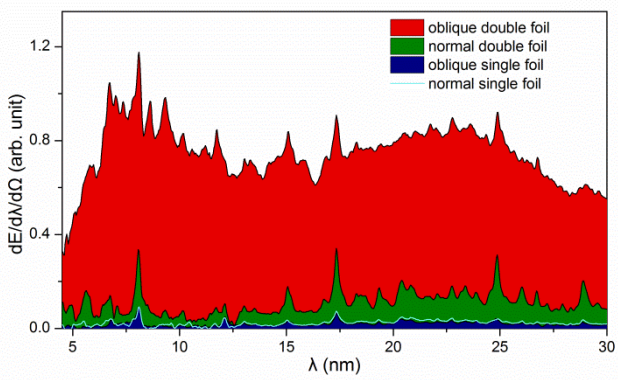

Figure 2.Measured spectra from 4 nm to 30 nm for different targets under different incidence.

As mentioned before, the angular distribution of the XUV emission can be characterized with the multi-angle transmission grating spectrometer. A full width at half maximum (FWHM) of 56 mrad for the emission from oblique double foil (ODF) is extracted from the data, which is of the same order as typical divergence of high-order harmonics generation from solid-density-plasma surfaces. By integrating the intensity over frequency and taking into account the divergence, it is found that the XUV energy from 18 eV to 280 eV in the case of ODF is 15 μJ, 3 order of magnitude larger than the current state-of-art energy of isolated attosecond pulses from gas harmonics.

Simulation

To gain insight into the dynamics of the generation of FRES under our experimental condition. 2D particle-in-cell (PIC) simulations were performed. It is found that a high-density relativistic electron sheet with forward momentum of about $\mathbf{10}\boldsymbol{mc}$ can be generated under experimental parameters. In front of the second foil, the FRES gains a transverse momentum of about $\mathbf{1.3}\boldsymbol{mc}$ from the obliquely reflected drive pulse. Figure 3 shows the FRES just after it passes the second foil.

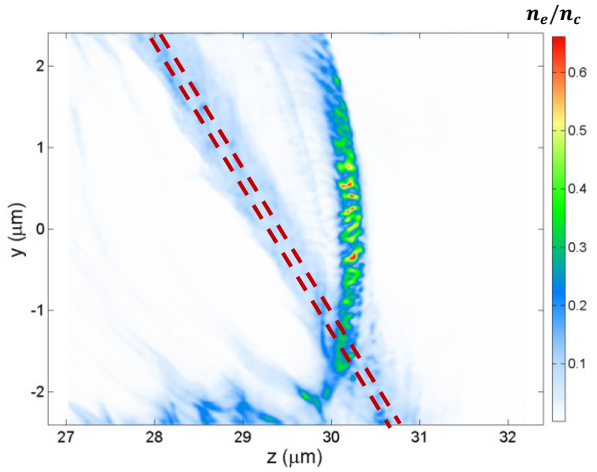

Figure 3. 2D simulation results under experimental condition. The color scale shows the electron density. The red dashed line marks the second foil. For a better vision, the electrons of the second foil are not shown.

Conclusion

The idea of generating a half-cycle isolated attosecond pulse from a sliding relativistic electron has been experimentally realized with currently available laser and target technology. The continuum spectra, extending up to 280 eV photon energy, suggest a duration of a few 100 as, and the total energy of about 15 μJ indicates electric field strength above 10^{12} V/m. The high brightness, small divergence and unipolar field feature of SRES emission make it highly attractive as light source for attosecond-pump attosecond-probe experiments. The high energy may allow single shot temporal characterization of the radiation. In the future, if electron sheets with larger forward momentum and higher density can be generated possibly through 1D wakefield acceleration, the duration of the radiation may be further compressed even below attosecond scale.

Acknowledgements

The authors would like to acknowledge the dedicated support of the Gemini laser staff and the CLF technical support.

References

1 Y. Nomura, et al., Nat Phys **5**, 124 (2009).
2 B. Dromey, et al., Nat Phys **5**, 146 (2009).
3 F. Quere, et al., Nat Phys **3**, 424 (2007).
4 U. Teubner and P. Gibbon, Rev Mod Phys **81**, 445 (2009).
5 G. Sansone, L. Poletto, and M. Nisoli, Nat Photonics **5**, 656 (2011).
6 V. V. Kulagin, V. A. Cherepenin, M. S. Hur, and H. Suk, Phys Rev Lett **99** (2007).
7 J. Meyer-ter-Vehn and H. C. Wu, Eur Phys J D **55**, 433 (2009).
8 D. Kiefer, et al., Nat Commun **4**, 1763 (2013).
9 H. C. Wu and J. Meyer-ter-Vehn, Nat Photonics **6**, 304 (2012).

Radiation Pressure of Relativistically Intense Lasers

Contact *m.streeter09@imperial.ac.uk*

M.J.V.Streeter and Z. Najmudin.

Blackett Laboratory, Imperial College London, London SW7 2AZ, UK

J.H. Bin, C. Kreuzer, W.J. Ma, J. Meyer-ter-Vehn, J. Schreiber.

Department of Physics, Ludwig-Maximilians-University, 80539 Munich, Germany
Max-Planck-Institute for Quantum Optics, D-85748 Garching, Germany

S. Cousens, B. Dromey, M. Yeung, M. Zepf.

Department of Physics and Astronomy, Queen's University Belfast, Belfast, BT7 1NN, UK

P.S. Foster, P.P. Rajeev, C. Spindloe.

Central Laser Facility, STFC Rutherford Appleton Laboratory, Chilton, Didcot, OX11 0QX, UK

Introduction

Laser-plasma interactions are now possible with pulse intensities in excess of 10^{20} Wcm^{-2}, opening up new mechanisms of ion acceleration. In almost all experiments to date the dominant process of ion acceleration from solid density targets has been sheath acceleration [1], whereby energetic electrons, produced at the laser-plasma boundary, expand outwards and create electrostatic fields at the plasma-vacuum interfaces. These fields accelerate ions away from the target to energies of >MeV per nucleon. For thick targets, electrons gain energy while in the focal region of the laser but are quickly shielded from the accelerating fields by the bulk of the plasma. For very thin targets (on the order of a few skin depths) the laser field can effectively accelerate electrons throughout the entire depth of the plasma for the duration of the pulse ($\boldsymbol{\tau}$). For this mechanism, termed radiation pressure acceleration (RPA) [2], laser energy is more efficiently converted to the energy of the ions ($\boldsymbol{\varepsilon_i}$), which scale with intensity ($\boldsymbol{I}$) and the areal density ($\boldsymbol{\sigma}$) of the target as,

$$\boldsymbol{\varepsilon_i = \frac{m_i}{2}\left[\frac{\tau I}{c\sigma}(1+R)\right]^2},$$

in the non-relativistic case, where R is the reflectivity of the laser. This compares favorably with the $(\boldsymbol{I\lambda})^{\frac{1}{2}}$ scaling seen for sheath acceleration. However, for currently available laser systems the maximum achievable ion energies by either sheath acceleration or RPA are similar. An intermediate process, which can also lead to the acceleration of ions is hole-boring acceleration, during which the radiation pressure drives the laser-plasma boundary into the target. Ions are reflected by the electro-static field at this boundary to twice the hole-boring velocity (v_{hb}), giving an ion energy of,

$$\boldsymbol{\varepsilon_i = \frac{I(1+R)}{cn_i}},$$

where (n_i) is the ion number density.

It is typically difficult to determine exactly which mechanisms have lead to an experimentally observed ion spectra due to the complex and time-varying nature of the interaction. For thin targets it is likely that a combination of all of these mechanisms are involved so more information about the dynamics of the laser-plasma interaction is required in order to characterise and optimise the resultant ion beams.

Signatures of RPA and hole-boring acceleration are recorded by the reflected laser pulse, due to the motion of the laser-reflecting surface. Previous experimental work has used the reflected laser spectrum to determine the surface acceleration [3]. However, a number of assumptions are required in order to obtain quantitative results and as such this approach can yield only an approximate answer. More recent results [4] have used a frequency-resolved optical gating (FROG) diagnostic to obtain the time-resolved second harmonic emission spectrum from a 1.4 ps interaction at 5×10^{19} Wcm^{-2}. This allows a much more qualitative determination of the target evolution during the interaction by tracking the front surface motion.

Here, we report on measurements of the motion of the laser-reflecting surface during the interaction of the Astra Gemini Laser with diamond-like carbon (DLC) [5] targets at a peak intensity of 2×10^{20} Wcm^{-2}.

Experimental setup

The experiment was performed using a single beam of the Astra Gemini laser at the Rutherford Appleton Laboratory. Each pulse initially contained ≈ 8 J and had a pulse length of 50 fs (FWHM). Double plasma mirrors were used to enhance the contrast to 10^{10} with a throughput of 50% resulting in ≈ 4 J on target. An f/2 off-axis parabola was used to create a 3.5 µm focal spot (FWHM) containing 25 % of the pulse energy. Diamond-like carbon (DLC) targets of thickness 3.5 - 1000 nm were shot at 0 degrees angle of incidence and with linear polarisation. The focusing parabola had a central 1 cm diameter hole, which was used to sample the backscattered laser energy. Two Grenouilles [6] (commercial FROGs based on second harmonic generation) were used to characterise the temporal properties of the backscattered pulse. An optical spectrometer also measured the time-integrated spectrum of the backscattered radiation. A layout of the experiment is shown in figure 1.

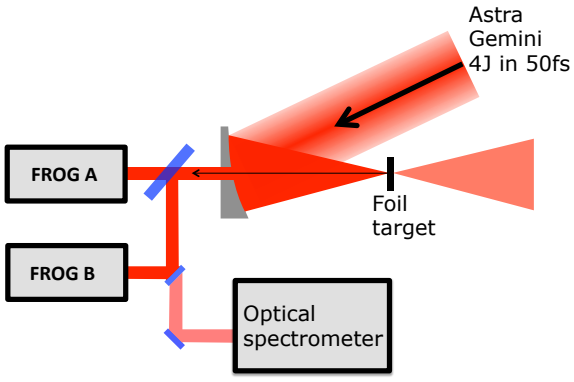

Figure 1: A schematic of the experimental setup showing the FROG diagnostics.

Results

FROG images of the backscattered pulses were recorded and the pulse profiles were retrieved for each shot and compared to determine the temporal profile of the laser pulse after the interaction. For each shot there were two possible retrieved pulses for each FROG, due to the time direction ambiguity of the autocorrelation process. However there was an extra 5.5 mm

of fused silica in the path to FROG A compared to FROG B. Therefore, by mathematically back-propagating both potential solutions for the FROG A pulses through this extra glass it is possible to determine the correct direction of time. This is most easily seen through the Wigner distribution [7], which gives a visual representation of the time dependant spectrum of the pulse. Figure 2 shows the Wigner distributions for both potential retrieved pulse shapes from each diagnostic. By comparing the images it is seen that the pulse is negatively chirped and so the time-direction ambiguity of the diagnostic is removed.

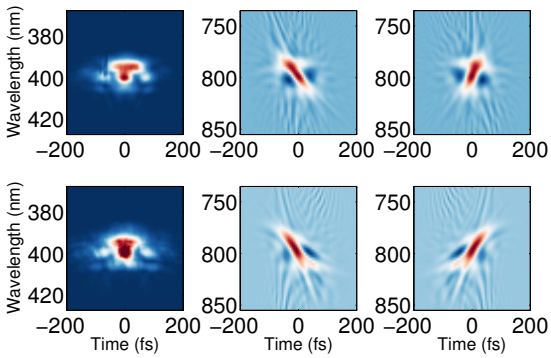

Figure 2: Wigner distributions of the potential retrieved pulse fields from (top) FROG A and (bottom) FROG B. Negative on the x axis corresponds to early times.

The central frequency as a function of time was found by determining the centre of weight of the Wigner distribution at each time over the region where the pulse intensity falls to half of the maximum. Assuming that the frequency shift of the pulse is entirely due to the motion of the reflecting surface the recession velocity is given by $\boldsymbol{v/c = (\omega_i - \omega_r)/\omega_r}$, where $\boldsymbol{\omega_i}$ and $\boldsymbol{\omega_r}$ are the frequency of the incident and reflected pulses respectively. The incident pulse was measured to have a negative chirp so $\boldsymbol{\omega_i}$ also varies in time. For all pulses $\boldsymbol{t = 0}$ was set at the maximum of the pulse envelope and the surface velocities obtained are shown in figure 3.

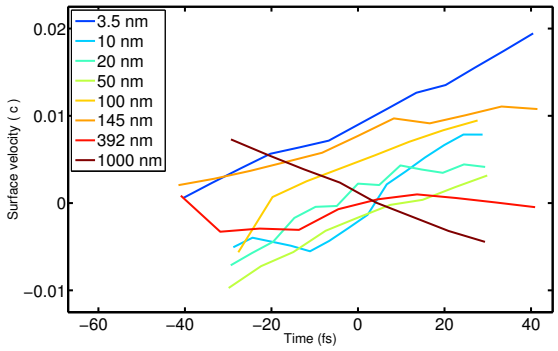

Figure 3: The velocity of the laser-reflecting surface as a function of time for DLC targets. Positive velocities are in the forward direction of the incident laser.

The surface velocities of the targets show significant variation in their absolute position but the slope of the lines clearly varies over the thickness range. The 1000 nm target shows an initial recession from the laser but as the interaction progressed this switched to motion towards the laser. For targets below 145 nm in thickness the acceleration is observed in the opposite direction. The range of initial observed velocities indicates that various different behaviours are possible before the peak of the pulse arrives. This is likely due to fluctuations in the laser temporal and spatial characteristics between each shot. The average acceleration for each shot is plotted against target thickness in figure 4. This shows a clear trend for thinner targets to experience a much stronger acceleration away from the laser. A linear fit of the form $\dot{\boldsymbol{v}}(\boldsymbol{d}) = \dot{\boldsymbol{v}}_{\boldsymbol{0}} + \boldsymbol{md}$ was found for $\dot{\boldsymbol{v}}_{\boldsymbol{0}} = 0.565 \times 10^{20}$ ms^{-2} and $\boldsymbol{m} = -1.6 \times 10^{17}$ ms^{-2} nm^{-2} with an RMS error of 0.164. The existence of negative accelerations demonstrates that pure light-sail acceleration is does not occur for the thicker targets. For the 3.5 nm target the simple 1D light-sail model would obtain a much higher acceleration than observed. This indicates that the acceleration measured is a result of the balance between the radiation pressure and the plasma pressure. In addition, the peak proton energies observed during the experiment were 5-10 MeV, much higher than would be expected from the hole-boring or light-sail mechanisms for the observed surface velocities.

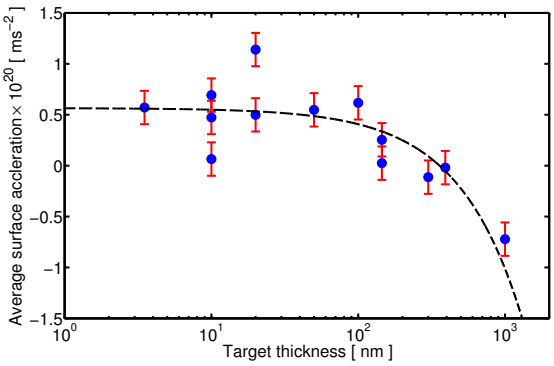

Figure 4: Average surface acceleration as a function of DLC target thickness.

Determining the plasma temperature

The plasma pressure can be calculated by equating the forces and accelerations at the reflecting surface,

$$\frac{\boldsymbol{I}}{\boldsymbol{c}}(\boldsymbol{1 + R - L}) - \frac{\boldsymbol{3}}{\boldsymbol{2}}\boldsymbol{n_e k_b T_e} = \frac{\boldsymbol{M}}{\boldsymbol{A}}\dot{\boldsymbol{v}}$$

where $\boldsymbol{I}$ is the laser intensity, $\boldsymbol{R}$ is the surface reflectivity and $\boldsymbol{L}$ is the surface transparency. The quantity $(\boldsymbol{R - L})$ was estimated as 0.65 from measurement in previous experiments [8] and $\boldsymbol{L}$ was calculated from the expanded target skin depth and thickness. The intensity used was the pulse FWHM averaged intensity of 2×10^{20} Wcm^{-2}. The accelerated mass, $\boldsymbol{M}$, was estimated as the mass in a cylindrical volume $\boldsymbol{V}$ of cross section $\boldsymbol{A}$ and thickness of the skin depth or the target thickness if that was smaller.

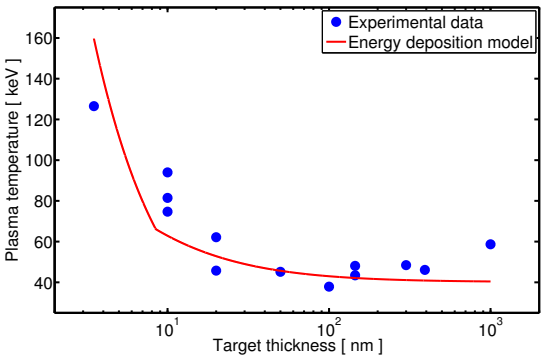

Figure 5: Plasma temperature calculated from the experimentally observed surface acceleration alongside the calculated temperature from the laser absorption into a cylindrical volume of 55 μm**.**

The target temperature can also be estimated by the absorbed laser energy in the cylindrical volume $\boldsymbol{V}$. This estimated plasma temperature and that found from the measured surface acceleration and target densities are plotted in figure 5 and show an approximate agreement for a cylinder radius of 55 μm.

Simulations

For a plasma with a front surface density gradient, the laser reflects from all regions above the critical density ($\boldsymbol{n_c}$). The proportion of energy reflected as the laser propagates is given by the complex index of refraction. So for a diagnostic measuring the Doppler shift of a laser reflecting from a complex plasma target there is a question over what surface is actually being tracked. A 2D3V particle-in-cell (PIC) simulation was performed using the code OSIRIS [9] to determine how the reflected laser is modified by the time-varying target density profile. Figure 6 shows the evolution of an initially 35 nm target with $\boldsymbol{n_e = 257\, n_c}$. The position of one skin depth into the plasma is calculated from the density profile at each time step, as is the relativistic skin depth for $\gamma = \sqrt{\boldsymbol{a_0^2/2 + 1}}$, where a_0 is given by the incident laser intensity. The laser-reflecting surface is found by measuring the time-dependant frequency of the reflected laser pulse. It is observed that the target expands from both the front and rear surfaces with the peak density position moving away from the laser. The laser reflecting surface remains comparatively stationary during this time and falls between the relativistic and non-relativistic skin depth surfaces.

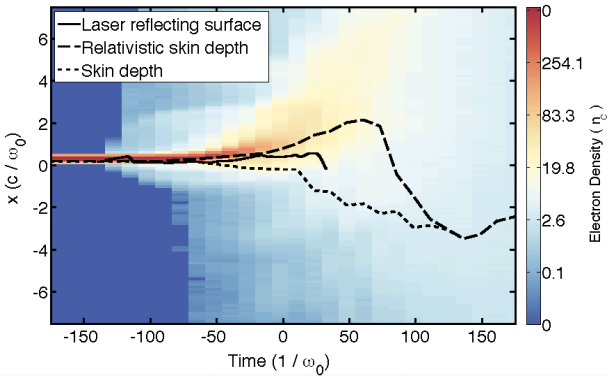

Figure 6: Longitudinal density profile as a function of time during an OSIRIS PIC simulation. Zero on the time axis corresponds to the peak of the incident laser pulse reaching the initial target surface.

Conclusion

Experimental measurements of the laser-reflecting surface motion has shown accelerations of up to 0.5×10^{20} ms^{-2} during the interaction of high-intensity (2×10^{20} Wcm^{-2}) 50 fs pulses with nm-scale targets. These measurements show that a simple light-sail model is inadequate to describe the interactions, while equating the laser and plasma pressures to the observed acceleration indicates a plasma temperature of ~100 keV.

The maximum observed surface recession velocity of $0.02\,c$ would correspond to proton energies of 1.7 MeV if accelerated by the hole-boring mechanism. This is considerably lower than observed in the experiment, demonstrating that hole-boring can only account for the lower energy part of accelerated ion spectra. Therefore, an electrostatic sheath acceleration mechanism is most likely dominant in these interactions.

Acknowledgements

The authors are very grateful for the excellent work of the CLF staff particularly those who ran the laser and provided technical support for the experiment.

References

1. E. L. Clark, *et al*., *Physical Review Letters*, **85** 1654–1657 (2000)
2. J. Fuchs *et al*., *Physical Review Letters* **94** 045004 (2005)
3. R. Sauerbrey, *Physics of Plasmas* **3** 4712 (1996)
4. Y. Ping et al., *Physical Review Letters* **109** 145006 (2012)
5. W. Ma *et al*. *Nucl Instr Meth A* **655**, 53-56 (2011).
6. D. J. Kane and R. Trebino, *Optics Letters* **18** 823 (1993)
7. E. Wigner, *Physical Review* **40** 749–59 (1932)
8. M. J. V. Streeter *et al*., *New Journal of Physics* **13** 023041 (2011)
9. R. Fonseca, L. Silva, F. Tsung and V. Decyk, *Lecture Notes in Computer Science* **2331** 342–51 (2002)

Hole-boring at high intensity in near-critical density targets

Contact *jinqing.yu@imperial.ac.uk*

Jinqing Yu

The John Adams Institute for Accelerator Science, Blackett Laboratory, Imperial College London, SW7 2AZ, UK and Vacuum Electronics National Laboratory, University of Electronic Science and Technology of China Chengdu, 610054, People's Republic of China

N. P. Dover, A. E. Dangor and Z. Najmudin

The John Adams Institute for Accelerator Science, Blackett Laboratory, Imperial College London, SW7 2AZ, UK

Xiaolin Jin and Bin Li

Vacuum Electronics National Laboratory, University of Electronic Science and Technology of China Chengdu, 610054, People's Republic of China

Introduction

Ultra-intense laser–plasma interactions are a well-known source of multi-MeV protons and ions. High-quality ion bunches in the 100–1000 MeV range are motivated by a number of possible applications such as medical hadron therapy. One of the most significant current challenges is to generate high energy ion beam with narrow energy spread [1].

In the past few years, hole-boring radiation pressure acceleration (HB-RPA)[2-5] has generated great interest. Theoretical and experimental studies have been reported to enhance our understanding of HB-RPA mechanism.

In this report we discuss the generation of high quality proton beams from HB-RPA using two-dimensional Particle-in-Cell simulation. It is found that the energy spectrum of the proton beam has a sharp spike at more than 200 MeV with an energy spread less than 1% by 4.0×10^{22} W/cm^2 laser pulse. To further elucidate the generation and control of this spectral peak, a series of simulations were carried out to consider the effect of laser pulse intensity, pulse duration and plasma density on proton peak energy and energy spread.

Simulation conditions

A λ=1μm circularly-polarized laser pulse with Gaussian transverse and temporal laser profile with pulse lengths from 5 to 50 fs (full-width half maximum (FWHM)) duration and focal spot of 2.5 micron (FWHM) was introduced along the laser-axis from the left. The laser intensity was varied from 5.0×10^{21} W/cm^2 to 3.2×10^{23} W/cm^2. The plasma was initialized as fully ionized hydrogen. The initial density of the plasma was varied from 5 n_c to 50 n_c. The targets are 20 micron thick (longitudinal direction) and 40 micron wide (transverse direction).

High quality proton beam

Initially, the laser pulse length was 35 fs with an intensity of 4.0×10^{22} W/cm^2. The density of the plasma was 5 n_c. Figure 1 shows the proton energy spectrum at the time of 100 fs, well after the end of the laser plasma interaction. From this picture, one can see that there is a sharp spike (peak energy) in the spectrum at 235MeV with an energy spread less than 1%. Figure 2 shows the proton density at the same time. The proton beam with the sharp spike energy is located in the front of the proton beam as shown in the right-hand of the figure.

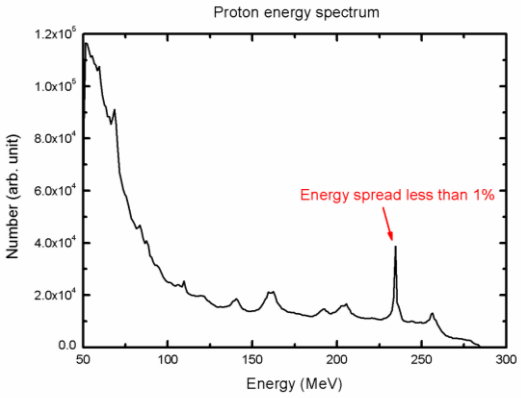

Figure 1. Proton energy spectrum at the end of the simulation for a pulse length of 35 fs and initial density 5 n_c.

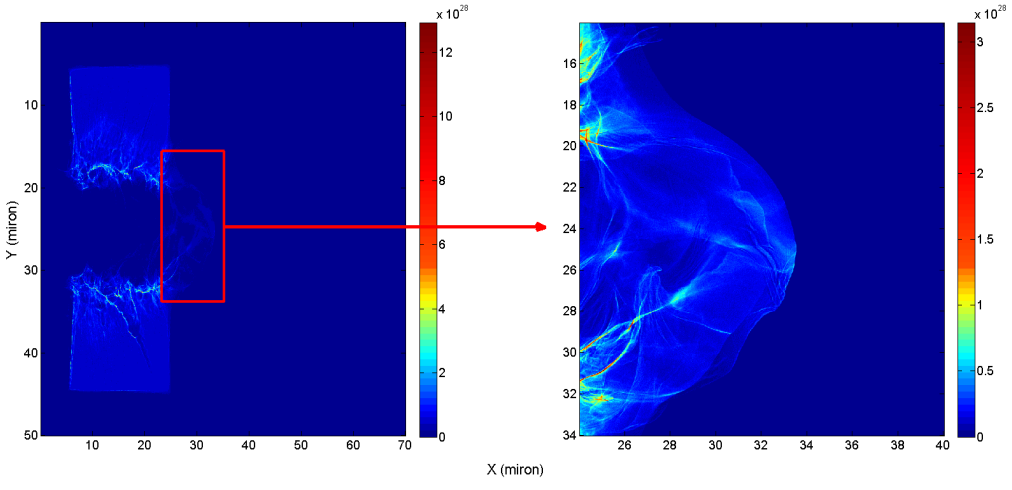

Figure 2. Proton density at the end of the simulation.

Changing laser pulse duration, pulse intensity and plasma density

To understand more about the sharp spectral features shown in figure 1, the laser pulse duration was varied from 5 to 50fs (FWHM). The laser intensity was varied from 5.0×10^{21} W/cm^2 to 3.2×10^{23} W/cm^2, and plasma initial density is from 5 to 50 n_c. Figure 3 shows the proton peak energy (not cut off energy) distribution due to changing the laser pulse duration, pulse intensity and plasma density. An absence of a point indicates that there is no high quality proton beam with narrow energy spread at that condition. Figure 4 shows the energy spread of the peak due to changing the simulation conditions. From figure 3, one can see that proton peak energy is determined by laser intensity, pulse duration and plasma density. Peak energy seems to inverse proportion to laser pulse duration for low plasma density (5 n_c or 10 n_c), while direct proportion to laser pulse duration for high plasma density (40 n_c or 50 n_c). For low intensity, low plasma density (10 n_c) is more adaptive to receive high quality proton beam of narrow energy spread as shown in figure 4. Higher intensity (near 10^{23} W/cm^2) is more suitable for HB-RPA, but Cattani's energy scaling [6] ($\sim(a_0)^{3/4}$) seems cannot work any more.

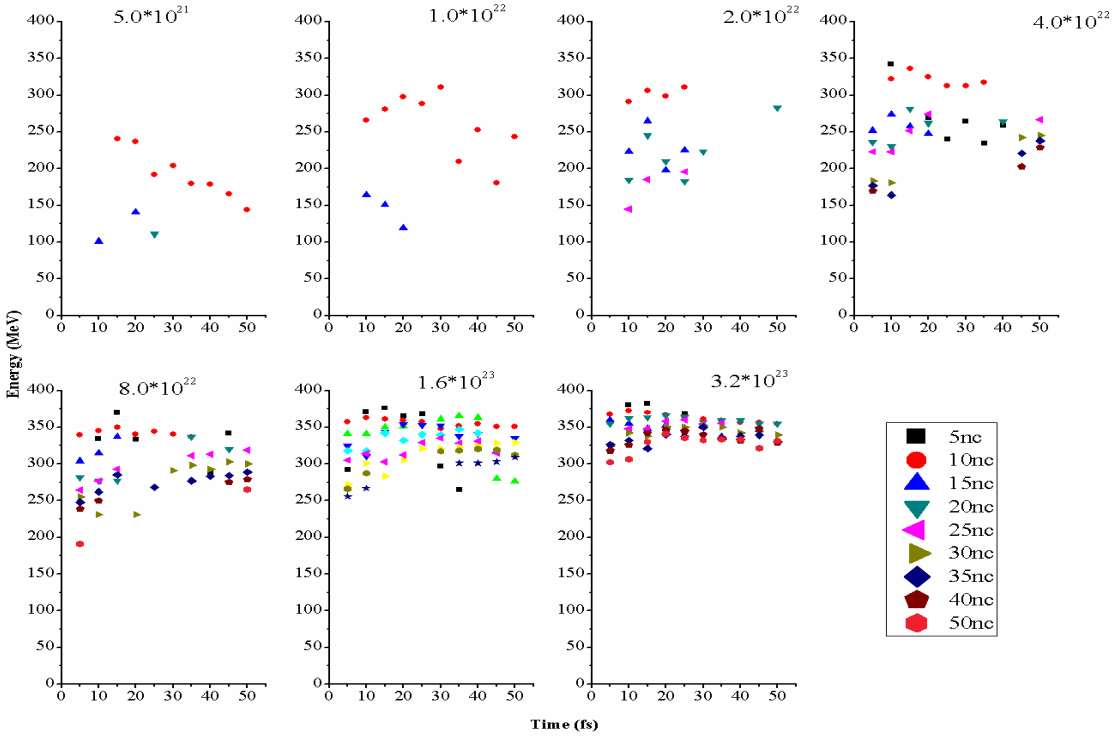

Figure 3. Variation of energy of the spectral peak with changing pulse length, intensity and initial plasma density.

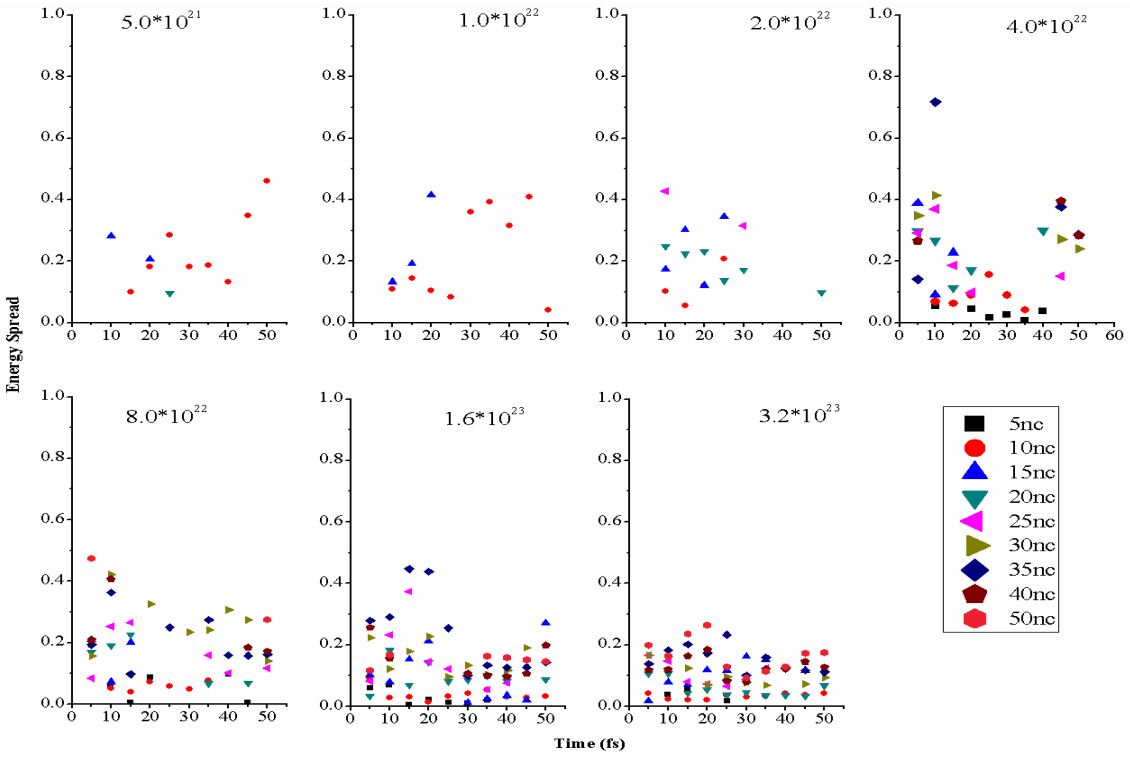

Figure 4. Variation the energy spread of the spectral peak with changing pulse length, intensity and initial plasma density.

Conclusions

We have studied proton acceleration from an ultra-intense laser pulse interacting with a near-critical density target using 2D-PIC simulations. The proton beam can be accelerated to more than 200MeV with energy spread less than 1%. We also consider the effect of laser pulse intensity, pulse duration and plasma density on proton peak energy and energy spread. This work may serve to improve the understanding of hole-boring acceleration.

Acknowledgements

Jinqing Yu wants to say thanks to the Fundamental Research Funds for the Central Universities (Grant No. ZYGX2012YB023).

References

1. Charlotte A. J. Palmer, N. P. Dover, I. Pogorelsky, M. Babzien, G. I. Dudnikova, M. Ispiriyan, M. N. Polyanskiy, J. Schreiber, P. Shkolnikov, V. Yakimenko, and Z. Najmudin, ***Phys. Rev. Lett.*** **106**, 014801 (2011).
2. A. P. L. Robinson, ***Phys. Plasmas*** **18**, 056701 (2011);
3. A. P. L. Robinson, R. M. G. M. Trines, N. P. Dover and Z. Najmudin, ***Plasma Phys. Control. Fusion*** **54** 115001 (2012).
4. A P L Robinson, P Gibbon, M Zepf, S Kar, R G Evans and C Bellei, ***Plasma Phys. Control. Fusion*** **51** 024004 (2009).
5. Andrea Macchi, Federica Cattani, Tatiana V. Liseykina, and Fulvio Cornolti, ***Phys. Rev. Lett.*** **94**, 165003 (2005).
6. F. Cattani, A. Kim, D. Anderson, and M. Lisak, ***Phys. Rev. E.*** **62**, 1234-1237 (2000).